applied sciences

MDPI

Article

A Hybrid Spectral-Element and Finite-Element Framework for Three-Dimensional Full-Wave Seismoelectric Modeling in VTI Porous Media

Peiyue Liu [1,2], Zhanghui An [1,2,*], Yingying Fan [1,2], Yi Lin [1,2], Xiyu Cao [1,2] and Yangning Hou [1,2]

[1] Lanzhou Institute of Seismology, China Earthquake Administration, Lanzhou 730000, China; liupeiyue24@mails.ucas.ac.cn (P.L.); fyy416@163.com (Y.F.); linyi233@mails.ucas.ac.cn (Y.L.); caoxiyuw@163.com (X.C.); houyn1234@163.com (Y.H.)
[2] Gansu Lanzhou Geophysics National Observation and Research Station, Lanzhou 730000, China
* Correspondence: anzhanghui5@gsdzj.gov.cn

Abstract

Assessing the contribution of electrokinetic effects to seismic electromagnetic signals requires forward methods capable of simulating coupled responses in anisotropic formations and complex geological models. We extend a three-dimensional hybrid spectral-element–finite-element time-domain framework to vertically transversely isotropic (VTI) porous media, incorporating directional stiffness, permeability and tortuosity. After decoupling Pride's equations, the framework solves Biot's equations using explicit time discretization to obtain the filtration-velocity field, which supplies the current source for an implicit time discretization of Maxwell's equations to calculate the coseismic electric field. The sequential scheme permits separate time steps for the poroelastic and electromagnetic calculations. After verifying the accuracy of the implementation, we evaluated the framework through half-space simulations and a modified salt-dome example. The half-space results show that elastic anisotropy changes seismic waveform shape and the corresponding electric response even when electromagnetic transport coefficients remain unchanged. In the controlled comparisons, one axial parameter at a time is reduced by 20%: drained stiffness, permeability or tortuosity. Permeability and tortuosity changes produce displacement differences below 0.16%, with electric-field differences of 0.97–1.57% and 1.75–4.97%, respectively. These electric-field differences exceed the electric-waveform variations in the U0 case with the tested mesh and time-step refinements. Hydraulic perturbations therefore produce small displacement changes accompanied by more pronounced changes in the coseismic electric field. The modified salt-dome example simulates an irregular porous inclusion within a VTI background, showing localized electric responses and out-of-plane electric-field components where the corresponding displacement components are weak. A matched isotropic/VTI background comparison further quantifies the electric-waveform changes in the same salt-dome geometry. These comparisons characterize 20% single-parameter finite changes at one receiver for the prescribed model and source. The salt-dome results illustrate the spatial response of a complex model; quantitative field application requires calibration and comparison with observations using site-specific material parameters, source information and instrument responses.

Keywords: seismoelectric modeling; vertical transverse isotropy; poroelasticity; spectral-element method; finite-element time-domain method; electrokinetic coupling; full-wave electromagnetic modeling

Check for updates

Academic Editor: Cristina Sáez Blázquez

Received: 11 October 2026
Revised: 1 November 2026
Accepted: 5 November 2026
Published: 9 November 2026

Copyright: © 2026 by the authors. Licensee MDPI, Basel, Switzerland. This article is an open access article distributed under the terms and conditions of the Creative Commons Attribution (CC BY) license.

1. Introduction

Seismic waves in fluid-saturated porous media drive relative motion between the pore fluid and solid skeleton, generating streaming currents and electromagnetic fields. Pride [1] derived the governing equations for this electrokinetic coupling. Chen and Mu [2] observed electric fields accompanying acoustic waves and interface conversion responses in laboratory experiments. Investigating the contribution of this mechanism to complex seismic electromagnetic signals requires numerical tools that link seismic sources to coseismic electric responses in geological models.

In recent years, studies of seismic electromagnetic observations have further highlighted the need for electrokinetic forward modeling methods. For example, Gao et al. [3] simulated the electrokinetic response of the 2017 Jiuzhaigou earthquake. In addition to distinguishing among different physical mechanisms, interpreting observed signals requires the examination of how seismic sources, medium properties, and propagation processes affect electrokinetic responses. Ren et al. [4] simulated electrokinetic fields generated by finite faults in layered porous media. Sun et al. [5] performed electrokinetic simulations of a Kumamoto aftershock and found that incorporating an approximate treatment of scattering improved agreement between the simulated and observed magnetic-field records. Cheng et al. [6] developed an analytically based method for earthquake-generated seismic and electromagnetic fields in layered ocean models, examining the influence of seawater and interfaces on the predicted responses. These studies indicate that electrokinetic forward models capable of representing source characteristics and medium structure provide an important tool for linking physical coupling mechanisms to seismic electromagnetic observations.

To investigate the contribution of electrokinetic mechanisms to seismic electromagnetic signals, researchers have developed a range of analytical and numerical solution methods. Haartsen and Pride [7] obtained point-source solutions in layered media, and Garambois and Dietrich [8] used a generalized reflection–transmission method to calculate full-waveform conversions in layered porous media. Haines and Pride [9] developed a grid-based numerical method that first computes poroelastic motion and then obtains the electric response by solving a Poisson equation for the electric potential. This scalar-potential approximation simplifies electromagnetic-field calculations, but Gao et al. [10] pointed out that it may omit shear-wave-associated electric fields and alter interface responses. To describe the electromagnetic response of seismoelectric waves more completely, subsequent studies have therefore adopted full-wave numerical methods that retain the displacement-current term in Maxwell's equations, further extending the capabilities of electrokinetic forward modeling. Ji et al. [11] developed a high-order finite-difference scheme for time-dependent seismoelectric waves. Li et al. [12] proposed a time-domain finite-element method for the two-dimensional coupling of compressional and vertically polarized shear waves with transverse-magnetic fields and subsequently applied explicit poroelastic and implicit electromagnetic updates to three-dimensional models, including a modified salt-dome model [13]. Bucher et al. [14] used a two-dimensional frequency-domain finite-element formulation coupling acoustic and seismoelectric equations to study offshore responses involving non-horizontal seabeds and reservoir interfaces.

Recent laboratory and numerical studies have further examined the roles of material contrasts and layer geometry in seismoelectric conversion. Bernardo et al. [15] investigated conversion at poroelastic/elastic interfaces and the role of dielectric-permittivity contrasts. Martins-Gomes et al. [16] examined how layer thickness and fluid-conductivity contrasts affect interface responses. These studies motivate considering mechanical structure and electrical transport together when interpreting interface-associated signals.

Subsurface media may also be anisotropic. Their direction-dependent elastic and fluid-transport properties affect poroelastic-wave propagation and streaming-current gener-

ation, making seismic electromagnetic responses more complex. Investigating the contribution of electrokinetic mechanisms to observed signals therefore also requires consideration of medium anisotropy. Regarding the underlying theory, Thomsen [17] described elastic-wave propagation in weakly anisotropic media, and Cheng [18] derived constitutive relations for anisotropic poroelasticity. In seismoelectric experiments and simulations, Zhu et al. [19] measured directional differences in seismoelectric amplitudes in quartz sand with anisotropic permeability. Tohti et al. conducted two-dimensional vertically transversely isotropic (VTI) simulations [20] and three-dimensional orthorhombic simulations [21]. Han et al. [22] combined anisotropic poroviscoelasticity with a Cole–Cole conductivity model and subsequently investigated velocity and attenuation anisotropy in two- and three-dimensional media [23]. These studies provide theoretical and experimental support for incorporating direction-dependent medium properties into electrokinetic simulations. Most existing anisotropic seismoelectric simulations use finite-difference grids or are restricted to two dimensions, so irregular interfaces must be approximated on a regular grid. In this study, we extend the three-dimensional spectral-element and implicit full-wave finite-element framework developed by Liu et al. [24] from isotropic to VTI poroelastic media so that directional material properties are combined with the geometric flexibility of a finite-element discretization. The sequential explicit–implicit solution strategy is retained, while the constitutive and transport treatment is extended to account for directional stiffness, permeability and tortuosity.

We first used half-space simulations to assess the accuracy of the improved framework. We then used comparative simulations to examine the effects of elastic and hydraulic perturbations on displacement and electric fields separately. Finally, we used a modified salt-dome model from the Society of Exploration Geophysicists (SEG)/European Association of Exploration Geophysicists (EAEG) project to assess the method's ability to simulate coupled wavefields in complex media with irregular interfaces.

2. Materials and Methods

2.1. Coupled Poroelastic and Electromagnetic Model

Biot [25] formulated wave propagation in a fluid-saturated porous solid, and Pride [1] coupled poroelastic motion to electromagnetic fields through electrokinetic transport. We use this coupling in a fully saturated, linearly poroelastic medium with a common vertical symmetry axis for the elastic and transport tensors. We assume isotropic grains and pore fluid, small deformation and time-independent properties.

Let $\mathbf{u}$ and $\mathbf{u}_f$ be the solid and fluid displacements, $\mathbf{w} = \phi(\mathbf{u}_f - \mathbf{u})$ the porosity-weighted relative displacement, and $\mathbf{q} = \partial_t \mathbf{w}$ the filtration velocity, where ϕ is porosity. With bulk density $\rho = (1-\phi)\rho_s + \phi\rho_f$, the governing Equations are

$$\nabla \cdot \boldsymbol{\tau} + \mathbf{f}_b = \rho \frac{\partial^2 \mathbf{u}}{\partial t^2} + \rho_f \frac{\partial^2 \mathbf{w}}{\partial t^2}, \tag{1}$$

$$-\nabla P + \mathbf{f}_f = \rho_f \frac{\partial^2 \mathbf{u}}{\partial t^2} + \frac{\rho_f}{\phi} \mathbf{T}_\infty \frac{\partial^2 \mathbf{w}}{\partial t^2} + \eta_f \mathbf{K}^{-1} \frac{\partial \mathbf{w}}{\partial t}, \tag{2}$$

Here, $\boldsymbol{\tau}$ is total stress, P is pore pressure, and η_f is fluid viscosity. The force densities $\mathbf{f}_b$ and $\mathbf{f}_f$ are defined per unit bulk and pore-fluid volume, respectively. For the solid-frame moment-tensor source used here, $\mathbf{f}_b$ is the equivalent force distribution, and $\mathbf{f}_f = \mathbf{0}$ (Section 2.3). The grain and fluid densities are ρ_s and ρ_f. The permeability and tortuosity tensors are $\mathbf{K} = \mathrm{diag}(k_h, k_h, k_v)$ and $\mathbf{T}_\infty = \mathrm{diag}(T_h, T_h, T_v)$. Stress and pressure are expressed through the five independent VTI stiffnesses and the directional Biot coefficients. Appendix A gives the stress–strain relations, directional Biot coefficients and storage modulus used here, following Cheng's anisotropic poroelastic formulation [18].

We neglect electroosmotic feedback on the mechanical field and convert filtration velocity to streaming current using $\mathbf{J}_s = \eta_f \mathbf{L}\mathbf{K}^{-1}\mathbf{q}$. We retain fluid inertia in the mechanical equations and solve Maxwell's equations with induction and displacement current:

$$\nabla \times \mathbf{H} = \boldsymbol{\sigma}\mathbf{E} + \boldsymbol{\varepsilon}\frac{\partial \mathbf{E}}{\partial t} + \eta_f \mathbf{L}\mathbf{K}^{-1}\frac{\partial \mathbf{w}}{\partial t}, \tag{3}$$

$$\nabla \times \mathbf{E} = -\mu_0 \frac{\partial \mathbf{H}}{\partial t}. \tag{4}$$

The electric and magnetic fields are $\mathbf{E}$ and $\mathbf{H}$, and magnetic permeability is μ_0. We apply the static Pride transport relations separately along the principal directions as an effective closure for $\mathbf{L}$, $\boldsymbol{\sigma}$ and $\boldsymbol{\varepsilon}$. This directional extension and the viscous source approximation are modeling assumptions of the framework. Appendix A specifies the coefficients and their low-frequency, thin-double-layer and weak-feedback conditions.

2.2. Sequential SEM–FETD Solution

The numerical procedure follows the sequential SEM–FETD framework of Liu et al. [24], retaining its sequential coupling strategy while extending the material treatment to VTI. The changes concern the direction-dependent poroelastic constitutive coefficients, hydraulic tensors and transport closure. As shown in Figure 1, an explicit spectral-element calculation provides the poroelastic wavefield. The stored relative fluid–solid velocities are extracted at the required electromagnetic time levels and weighted by porosity to obtain filtration velocity. This field drives an implicit full-wave finite-element calculation of the electromagnetic potentials, which are solved using the MUltifrontal Massively Parallel sparse direct Solver (MUMPS) to recover the electric and magnetic fields. The derivation and implementation of the sequential coupling are described in detail by Liu et al. [24].

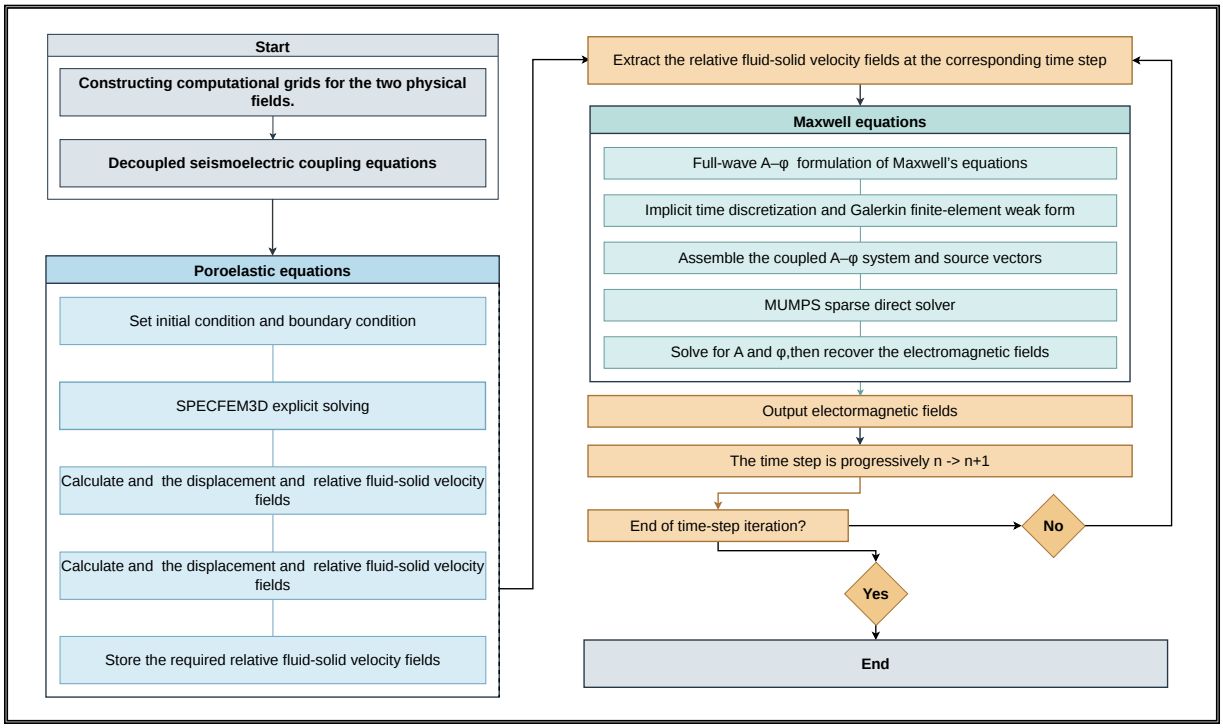


Figure 1. Sequential SEM–FETD workflow linking the poroelastic and electromagnetic calculations through the streaming-current source. Reproduced from Liu et al. [24].

Separate meshes represent the poroelastic and electromagnetic domains (Figure 2). The electromagnetic interior covers the seismic domain and extends into an air layer above and perfectly matched layers (PMLs) at the sides and bottom. Field transfer between the meshes connects the mechanical calculation to the electromagnetic current source.

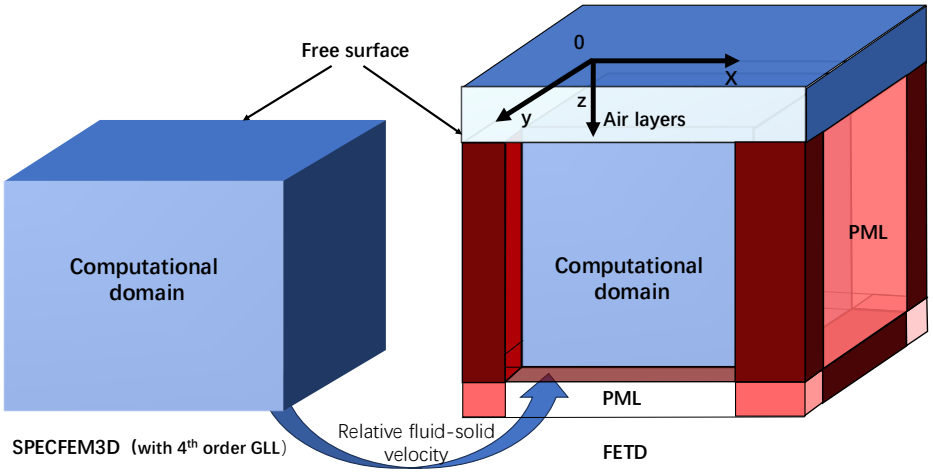


Figure 2. Poroelastic (**left**) and electromagnetic (**right**) domains. Blue: porous medium; light blue: air; red: PML. The arrow indicates relative fluid–solid velocity transfer. GLL: Gauss–Lobatto–Legendre nodes. Reproduced from Liu et al. [24].

Morency and Tromp [26] developed a spectral-element formulation for wave propagation in porous media. SPECFEM3D Cartesian (version 4.1.1) is an open-source spectral-element package for three-dimensional seismic-wave propagation in acoustic, elastic and poroelastic media. Founded by Dimitri Komatitsch and Jeroen Tromp, with development contributions from the French National Centre for Scientific Research (CNRS) and Princeton University, it is maintained by an international developer community [27]. The present method incorporates directional stiffness, fluid inertia and viscous resistance in SPECFEM3D, using fourth-degree Lagrange interpolation at Gauss–Lobatto–Legendre (GLL) nodes and explicit time integration. Filtration velocity is then interpolated to the electromagnetic quadrature points to construct the current source:

$$\mathbf{q}_e^{n+1} = \mathcal{I}_{p\to e}\mathbf{q}_{\mathrm{SEM}}^{n+1}, \qquad \mathbf{J}_{s,e}^{n+1} = \eta_f \mathbf{L}\mathbf{K}^{-1}\mathbf{q}_e^{n+1}. \tag{5}$$

The transport coefficients were evaluated within each material, and the source was synchronized with the electromagnetic time levels. The operator $\mathcal{I}_{p\to e}$ transfers the velocity between the two meshes.

For the electromagnetic solve, we used a magnetic vector potential $\mathbf{A}$ and electric scalar potential φ:

$$\mathbf{E} = -\frac{\partial \mathbf{A}}{\partial t} - \nabla\varphi, \qquad \mathbf{H} = \mu_0^{-1}\nabla \times \mathbf{A}. \tag{6}$$

These potentials were discretized using the Galerkin finite-element method with continuous nodal basis functions and implicit backward differences. The resulting first-order time scheme gives a coupled linear system for A_x, A_y, A_z and φ. MUMPS solves this system using the multifrontal algorithm described by Amestoy et al. [28]. The factorization is reused for fixed meshes, coefficients and the time step. Appendix C gives the potential equations, gauge treatment, time discretization and finite-element matrix assembly used in this electromagnetic solve.

We set the ground surface as a free surface and applied the first-order paraxial absorbing conditions of Clayton and Engquist [29] at the lateral and bottom seismic boundaries. No poroelastic displacement was computed in air. In the electromagnetic problem, the ground

surface is an air–earth material interface across which the fields satisfy electromagnetic continuity conditions; outgoing fields are absorbed in the PML. Both calculations started from rest. Spatial resolution must represent the shortest relevant directional wavelengths, while the explicit time step is constrained by the maximum wave speed and minimum GLL-node spacing. The implicit time step was selected to resolve the source bandwidth and electromagnetic variation. The interface, gauge and outer boundary conditions applied in these calculations are detailed in Appendix C.

2.3. Source Representation and Normalization

We imposed the isotropic explosive excitation through the moment-tensor source defined in the SPECFEM3D `CMTSOLUTION` file. The prescribed tensor amplitude is

$$\overline{\mathbf{M}} = M_{\mathrm{iso}}\mathbf{I}, \qquad M_{\mathrm{iso}} = 10^{15}\,\mathrm{dyne\,cm} = 10^{8}\,\mathrm{N\,m}, \tag{7}$$

i.e., equal diagonal components and zero off-diagonal terms. Here, M_{iso} is the amplitude of each diagonal component, not a separately defined scalar seismic moment; SPECFEM3D converts the input from dyne-centimeters to newton-meters [30].

The source-time multiplier is the unit-peak Ricker wavelet

$$s(t) = \left[1 - 2\pi^2 f_0^2 t^2\right]\exp\left(-\pi^2 f_0^2 t^2\right), \qquad f_0 = 1\,\mathrm{Hz}, \tag{8}$$

with t measured from the wavelet center and zero prescribed time shift, so $s(0) = 1$ and $\overline{\mathbf{M}}$ sets the amplitude.

For a source at $\mathbf{x}_s$, its equivalent bulk force is

$$f_{b,i}(\mathbf{x}, t) = -s(t)\sum_{j=1}^{3}\overline{M}_{ij}\frac{\partial}{\partial x_j}\delta(\mathbf{x} - \mathbf{x}_s), \qquad \mathbf{f}_f = \mathbf{0}. \tag{9}$$

SPECFEM3D assembles this point moment tensor through the spatial derivatives of the basis functions at the source location; for basis function N_a the load is

$$F_{ai}(t) = s(t)\sum_{j=1}^{3}\overline{M}_{ij}\frac{\partial N_a}{\partial x_j}(\mathbf{x}_s). \tag{10}$$

The weak form thus fixes the load from the moment tensor rather than an arbitrary nodal force. The tensor acts on the solid frame, with no independently imposed fluid-phase force, consistent with the SPECFEM3D poroelastic source assembly [30]; relative fluid motion follows from the coupled equations, and source-related terms in its acceleration update are not an additional external fluid force.

3. Results

We first define the homogeneous half-space setup and waveform measures. We compared the isotropic baseline against an independent reference solution and examine controlled 20% perturbations of three axial parameters. A salt-dome simulation then assessed coupled responses in complex media.

3.1. Half-Space Model and Accuracy Verification

We used the homogeneous half-space geometry shown in Figure 3, with a porous domain extending 16 km in each horizontal direction and 9 km in depth. We placed an isotropic explosive source S at (8.001 km, 8.001 km, 4 km) and receiver R, denoted T0 in the waveform comparisons, at (9.5 km, 9.5 km, 2.5 km). The z-axis points downward. The seismic mesh contains 147,456 hexahedral elements with a nominal size of 250 m. The electromagnetic mesh has 200,900 elements, including a 500 m air region and 750 m side and

bottom absorbing layers. We used a 1 Hz Ricker source and separate time steps of 0.002 s for the explicit poroelastic calculation and 0.020 s for the implicit electromagnetic calculation. The controlled parameter comparisons shared the same source, receiver T0, meshes and sampling arrangement.

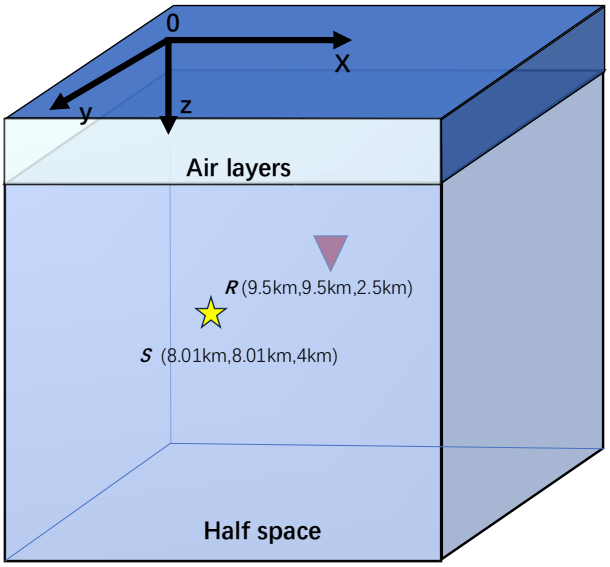


Figure 3. Homogeneous half-space model and source–receiver geometry. The light-blue upper layer represents air and the lower blue block the porous medium. The star and triangle mark source S and receiver R (T0). The revised parameter simulations used S at $(8.001, 8.001, 4)$ km and T0 at $(9.5, 9.5, 2.5)$ km; the source annotation in this inherited schematic refers to the original reference geometry. The z-axis is positive downward. Reproduced from Liu et al. [24].

For the controlled perturbations in Section 3.2, U0 denotes the isotropic baseline, with permeability 10^{-9} m^2 and tortuosity three in all directions. Appendix B provides the reference material and fluid-chemistry inputs, together with the resulting electromagnetic coefficients.

For each recorded component $a \in \{u_x, u_y, u_z, E_x, E_y, E_z\}$, the relative waveform difference was measured using

$$D_2^{(m)}(a; \mathcal{W}) = 100 \frac{\left[\sum_{n \in \mathcal{W}} (a_n^{(m)} - a_n^{(\mathrm{ref})})^2\right]^{1/2}}{\left[\sum_{n \in \mathcal{W}} (a_n^{(\mathrm{ref})})^2\right]^{1/2}}. \tag{11}$$

Here, m denotes the comparison case and $\mathcal{W}$ the set of samples included in the comparison. The complete record was used unless a time window is specified. U is the reference for the benchmark comparison, and U0 is the reference for the material comparisons. The plots also show signed residuals normalized by the corresponding reference peak. Appendix E specifies the displacement and electric-field sampling for the controlled parameter comparisons, and the residual normalization and peak measures used below.

As an independent check, we compared the U0 calculation with the reference solution obtained using the semi-analytical method of Hu and Gao [31]. The two calculations used the same material parameters, explosive source and source–receiver geometry. All three solid-displacement and all three electric-field components agree well in arrival time, phase and the relative amplitude of the dominant lobes (Figure 4), demonstrating the accuracy of the proposed method.

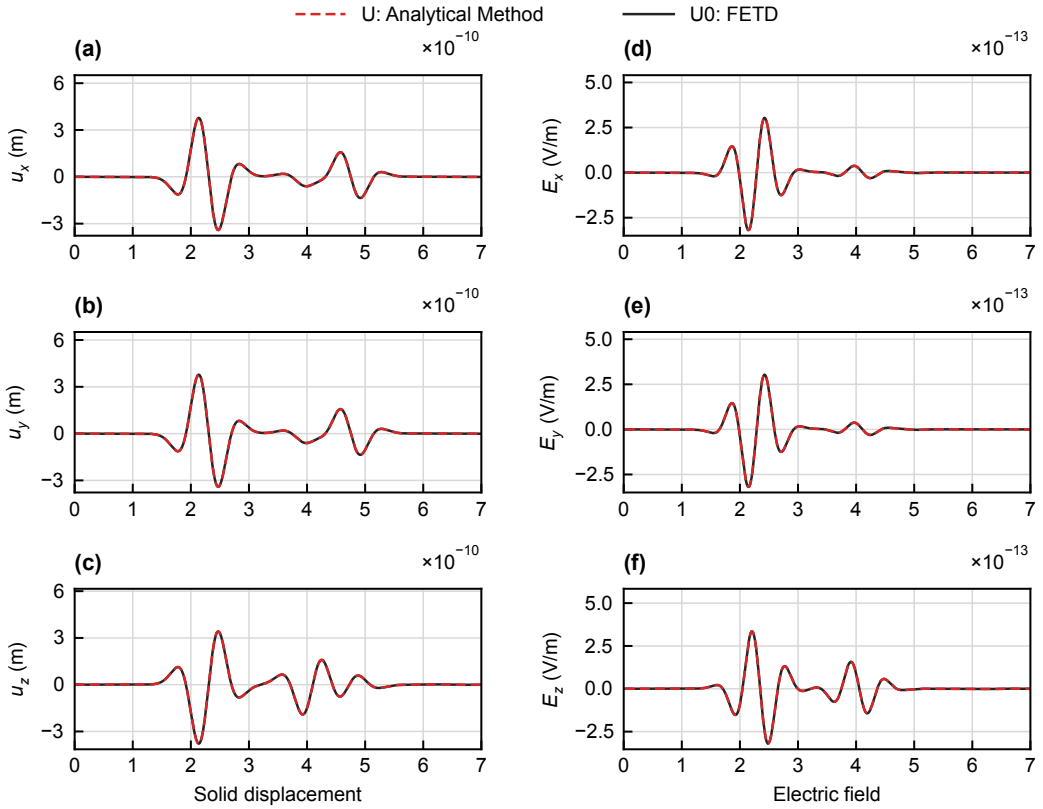


Figure 4. U0 verification at T0 against the semi-analytical reference of Hu and Gao [31]. Panels (**a**–**c**): displacement components; (**d**–**f**): electric-field components. Red dashed: reference U; black solid: present result U0.

3.2. Elastic and Hydraulic Anisotropy

Starting from the same isotropic reference U0, we decreased one independent axial parameter by 20% in each calculation: C_{33}^{d} in UE, k_v in UK and T_v in UT. All other independent material inputs remained fixed. The directional Biot coefficients, storage modulus and electromagnetic transport coefficients were recomputed from the adopted constitutive relations, rather than held fixed when their defining inputs changed. Table 1 specifies the inputs; Table 2 reports the waveform differences.

Table 1. Directional inputs of the controlled 20% comparisons. Stiffnesses are drained coefficients in GPa; $C_{12}^{d} = C_{11}^{d} - 2C_{66}^{d}$. Only C_{33}^{d}, k_v or T_v changes in UE, UK or UT, respectively.

Parameter	U0	UE	UK	UT
C_{11}^{d}	12.080000	12.080000	12.080000	12.080000
C_{33}^{d}	12.080000	9.664000	12.080000	12.080000
C_{44}^{d}	4.950000	4.950000	4.950000	4.950000
C_{66}^{d}	4.950000	4.950000	4.950000	4.950000
C_{13}^{d}	2.180000	2.180000	2.180000	2.180000
k_h (10^{-9} m^2)	1.0	1.0	1.0	1.0
k_v (10^{-9} m^2)	1.0	1.0	0.8	1.0
T_h	3.0	3.0	3.0	3.0
T_v	3.0	3.0	3.0	2.4

Table 2. Full-record relative waveform differences D_2 (%) for the controlled perturbations relative to U0.

Case	u_x	u_y	u_z	E_x	E_y	E_z
UE	47.1277	47.1419	66.0825	18.3508	18.3598	58.8173
UK	0.0886	0.0886	0.1566	0.9738	0.9745	1.5718
UT	0.0229	0.0226	0.1261	1.7543	1.7519	4.9709

To distinguish waveform-amplitude normalization from parameter normalization, we define the dimensionless finite-change sensitivity of component a to the single perturbed parameter p as

$$S_{a,p}^{(m)} = \frac{\|a^{(m)} - a^{(0)}\|_2 / \|a^{(0)}\|_2}{|\Delta p / p_0|} = \frac{D_2^{(m)}(a)}{20}, \qquad \Delta p / p_0 = -0.20. \tag{12}$$

Here D_2 is its numerical percentage value from Equation (11). This non-negative norm measures a finite waveform change per unit relative parameter change; it is neither a signed derivative nor an infinitesimal sensitivity. The residual curves remain normalized by the U0 component peak, as defined in Appendix E, and should not themselves be read as parameter sensitivities. The resulting sensitivities are summarized in Table 3.

Table 3. Dimensionless finite-change sensitivities $S_{a,p}$ for the common 20% decrease. Each row concerns one specified independent parameter.

Parameter	u_x	u_y	u_z	E_x	E_y	E_z
C_{33}^d	2.35639	2.35709	3.30413	0.91754	0.91799	2.94086
k_v	0.00443	0.00443	0.00783	0.04869	0.04872	0.07859
T_v	0.00114	0.00113	0.00631	0.08771	0.08760	0.24855

Reducing C_{33}^d in UE gives displacement differences of 47.128%, 47.142% and 66.083% in x, y and z; the corresponding electric differences are 18.351%, 18.360% and 58.817% (Figure 5). The dimensionless sensitivities are 2.356–3.304 for displacement and 0.918–2.941 for the electric field. Waveform changes are evident in the later lobes and residuals. The sampled displacement maxima shift by 0.008, 0.008 and 0.006 s; electric maxima shift by 0.020 s. These maxima identify dominant lobes and are not first-arrival picks.

For the 20% reduction in k_v (UK), displacement differences remain below 0.157%, whereas electric differences are 0.974%, 0.974% and 1.572% (Figure 6). Parameter-normalized values are 0.00443–0.00783 for displacement and 0.0487–0.0786 for the electric field. Electric peak magnitudes increase by approximately 0.447% in the horizontal components and decrease by 0.0492% vertically. The sampled peak times remain unchanged.

For the 20% reduction in T_v (UT), displacement differences are 0.0229%, 0.0226% and 0.1261%; electric differences are 1.754%, 1.752% and 4.971% (Figure 7). The dimensionless sensitivities are 0.00113–0.00631 for displacement and 0.0876–0.2485 for the electric field. The electric peaks change by approximately +0.634% horizontally and −0.0755% vertically, with no sampled peak-time change. Late-time electric residuals remain visible despite the small changes in peak magnitude. Appendix E reports the peak and time-window measures for all three comparisons.

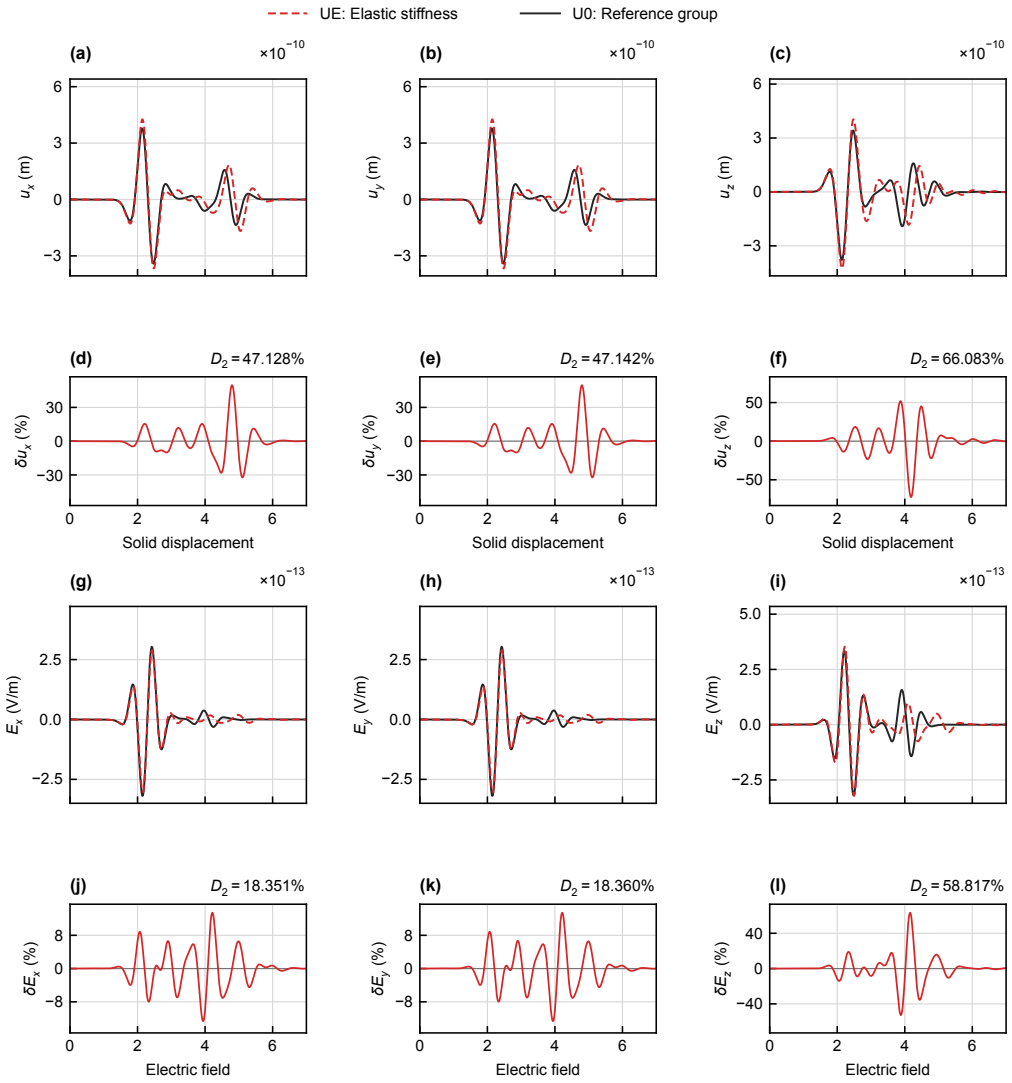


Figure 5. Elastic comparison at T0 for a 20% reduction in C_{33}^{d}. (**a**) u_x; (**b**) u_y; (**c**) u_z; (**d**) normalized residual of u_x; (**e**) normalized residual of u_y; (**f**) normalized residual of u_z; (**g**) E_x; (**h**) E_y; (**i**) E_z; (**j**) normalized residual of E_x; (**k**) normalized residual of E_y; (**l**) normalized residual of E_z. Black solid: U0; red dashed: UE. Residuals are normalized by the respective U0 peaks; annotations show full-record D_2.

3.3. Mesh and Time-Step Convergence Check

To assess the convergence of the half-space calculation we repeated the U0 model with the three mechanical meshes and two mechanical time steps listed in Tables 4 and 5: nominal element sizes of 250, 225 and 200 m at a fixed mechanical time step of 0.002 s, and time steps of 0.002 and 0.001 s on the 250 m mesh. All calculations retained the U0 material parameters, source, receiver and boundary configuration, and the electromagnetic mesh and step are identical, so the comparison isolated the mechanical discretization and shows how it propagates into the electric field.

We compared the vertical displacement and vertical electric-field peaks in the first dominant wave packet over the common window $\mathcal{W}_P = [3.00, 3.75]$ s of record time, without peak alignment or amplitude rescaling. The finest record of each series served only as the comparison reference. We define

$$A_P(a) = \max_{t_n \in \mathcal{W}_P} |a(t_n)|, \qquad a \in \{u_z, E_z\},$$
$$e_P(a) = 100 \frac{|A_P(a) - A_{P,\mathrm{ref}}(a)|}{A_{P,\mathrm{ref}}(a)}. \tag{13}$$

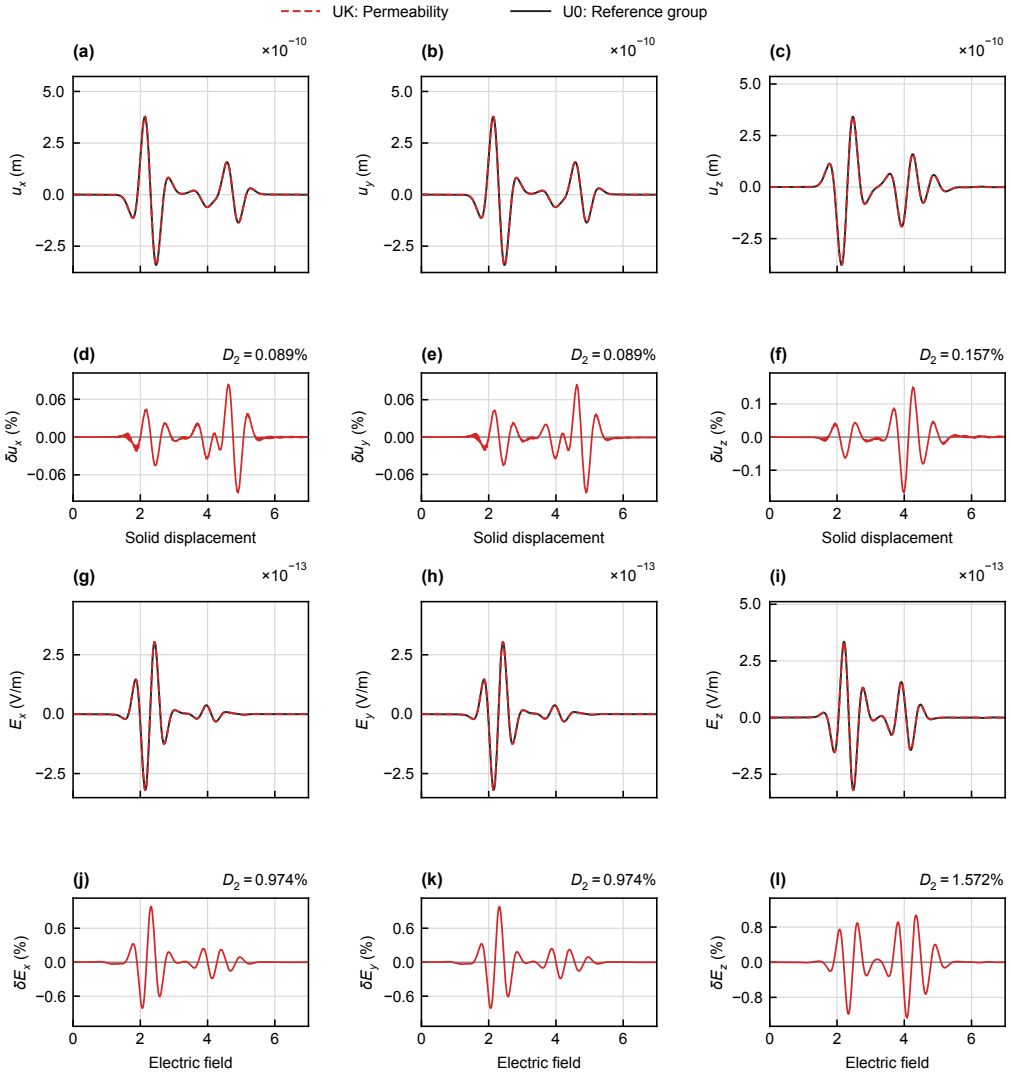


Figure 6. Permeability comparison at T0 for $k_v/k_h = 0.8$. (**a**) u_x; (**b**) u_y; (**c**) u_z; (**d**) normalized residual of u_x; (**e**) normalized residual of u_y; (**f**) normalized residual of u_z; (**g**) E_x; (**h**) E_y; (**i**) E_z; (**j**) normalized residual of E_x; (**k**) normalized residual of E_y; (**l**) normalized residual of E_z. Black solid: U0; red dashed: UK. Layout and normalization follow Figure 5.

Table 4. U0 mesh peak comparison. The mechanical time step is 0.002 s; A_P and e_P are defined in Equation (13). Relative peak differences use the nominal 200 m record as reference.

h (m)	Δt_{SEM} (s)	$A_P(u_z)$ (10^{-10} m)	$e_P(u_z)$ (%)	$A_P(E_z)$ (10^{-13} V/m)	$e_P(E_z)$ (%)
250	0.002	2.58797289	0.14653	2.10677180	0.17892
225	0.002	2.58835842	0.13166	2.10274154	0.01272
200	0.002	2.59177074	0.00000	2.10300910	0.00000

Table 5. U0 time-step peak comparison. The nominal mechanical mesh is 250 m; relative peak differences use the 0.001 s record as reference.

h (m)	Δt_{SEM} (s)	$A_P(u_z)$ (10^{-10} m)	$e_P(u_z)$ (%)	$A_P(E_z)$ (10^{-13} V/m)	$e_P(E_z)$ (%)
250	0.002	2.58797289	0.00384	2.10677180	0.17711
250	0.001	2.58787353	0.00000	2.10304703	0.00000

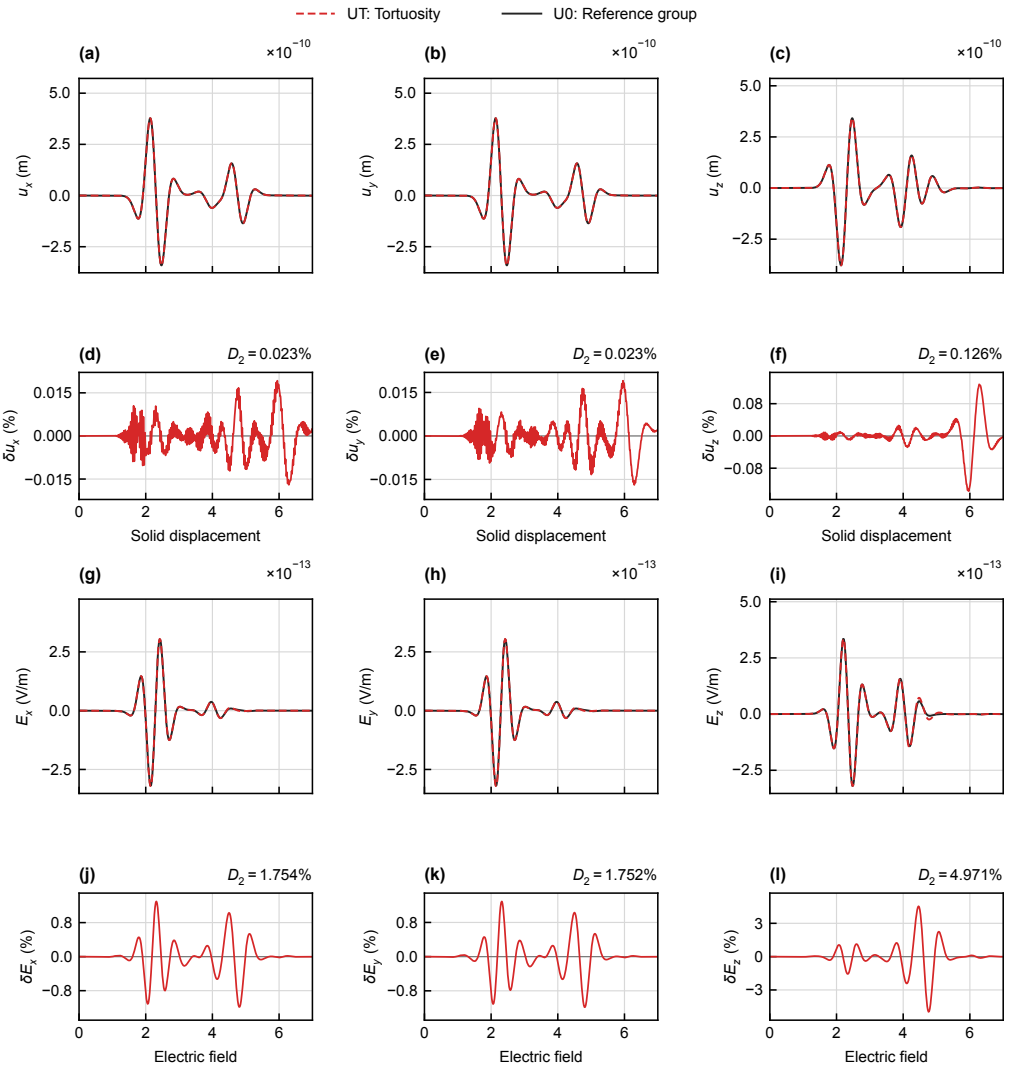


Figure 7. Tortuosity comparison at T0 for $T_h = 3$ and $T_v = 2.4$. (**a**) u_x; (**b**) u_y; (**c**) u_z; (**d**) normalized residual of u_x; (**e**) normalized residual of u_y; (**f**) normalized residual of u_z; (**g**) E_x; (**h**) E_y; (i) E_z; (**j**) normalized residual of E_x; (**k**) normalized residual of E_y; (**l**) normalized residual of E_z. Black solid: U0; red dashed: UT. Layout and normalization follow Figure 5.

Tables 4 and 5 show that mesh refinement and time-step halving change the peak amplitudes by less than 0.2%, while the full-record electric-field differences decrease with mesh refinement. For the measures examined, the 250 m mesh and 0.002 s time step therefore satisfy the numerical convergence requirements of this case. These variations are substantially smaller than the electric-field differences caused by the hydraulic perturbations in Section 3.2, supporting their interpretation as responses to changes in material parameters.

3.4. Modified SEG/EAEG Salt-Dome Model

To examine coupled wave propagation around an irregular interface, we used a modified version of the SEG/EAEG salt-dome model introduced by Aminzadeh et al. [32] (Figure 8). The model occupies a 16 km × 16 km × 16 km computational domain, with the salt body centered 4 km below the surface. The background and porous-inclusion properties and their material identifiers are listed in Appendix D. An isotropic explosive source was placed at horizontal coordinates (8.125 km, 8.125 km) and a depth of 8 km, with a 1 Hz Ricker wavelet and a mechanical time step of 0.002 s. Boundary conditions followed Section 2.2. The electromagnetic computational domain, including the air layer and PMLs, contained 357,894 hexahedral elements and approximately 1.43×10^6 degrees of freedom. The simulation was run on a workstation equipped with an Intel Core i7-12700F processor and 64 GB of RAM. MUMPS solved the electromagnetic linear system, reusing the LU factorization while the system matrix remained unchanged. Memory usage observed during LU factorization was approximately 54 GB. The explicit SPECFEM3D poroelastic calculation and the subsequent electromagnetic calculation each took approximately 2 h, giving a total runtime of approximately 4 h.

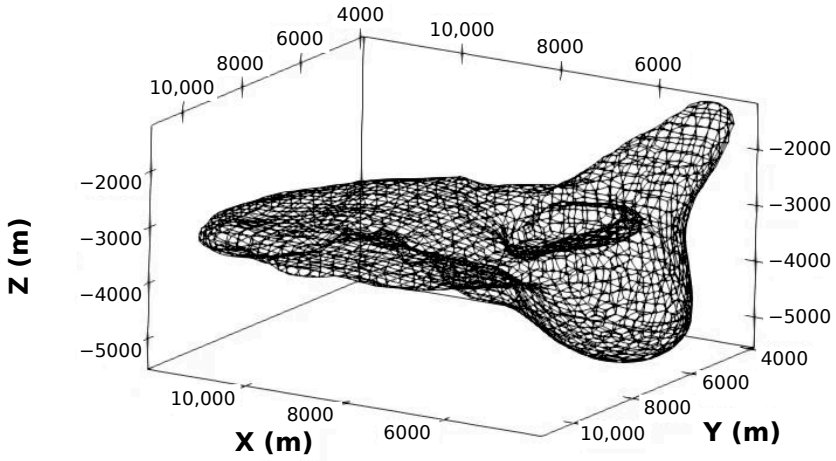


Figure 8. Geometry and burial position of the irregular porous inclusion in the modified SEG/EAEG salt-dome model. Coordinates are in meters; the vertical coordinate is elevation, with negative values below the surface. Reproduced from Liu et al. [24].

Figures 9–16 follow the displacement and electric fields in this simulation at 2.00, 2.80 and 3.60 s. The three-dimensional views in Figures 9 and 10 show the overall wavefield, while the paired displacement and electric-field maps in the *xz*, *xy* and *yz* sections reveal the response near different parts of the salt-dome boundary. Each section pairs the displacement with the electric field it generates so that the electric pattern can be compared directly with the mechanical field; the three sections sample the two vertical directions and the horizontal plane of the VTI background, and the three times cover the approach, intersection and passage of the main wavefront. To aid comparison, all displacement panels use a display range of $\pm 1.0 \times 10^{-10}$ m and all electric-field panels use $\pm 1.0 \times 10^{-13}$ V m^{-1}. Black contours in the vertical sections mark the salt-dome boundary. These sections use depth increasing downward; the three-dimensional views use elevation, with negative values below the surface.

The outer displacement wavefront is approximately elliptical in the *xz*-plane, whereas its horizontal extent is approximately circular in the *xy*-plane. This difference is most apparent away from the salt body. The horizontal displacement components have different lobe polarizations but comparable radial extents. This contrast is consistent with the vertical–horizontal propagation difference and horizontal rotational symmetry of the

VTI background. The xz- and yz-slices also show different salt-dome boundary shapes, with corresponding differences in the upper wavefronts and the fields near the interface.

At 2.00 s, the seismic wavefront approaches the irregular lower boundary. The electric field includes both a response following the mechanical wavefront and localized patches near the salt body. At 2.80 s, the wavefront intersects the inclusion, and its upper part becomes irregular. Alternating positive and negative electric-field patches appear along the curved boundary and within the inclusion.

At 3.60 s, the main wavefront has passed through most of the salt body, leaving distorted upper displacement lobes and secondary structures behind it. The electric field retains a broad propagating response together with localized positive and negative regions near the inclusion. In the vertical slices, E_y in the xz-plane and E_x in the yz-plane remain visible where the corresponding displacement components are weak. In the xy-plane, the horizontal electric-field components extend laterally, whereas E_z becomes less conspicuous at later times within the fixed display range. Taken together, the figures show that the extended framework retains the irregular-interface capability of the finite-element formulation and adds the directional propagation of a VTI background that the previous isotropic implementation did not represent. Section 4 discusses their implications for electrokinetic signals.

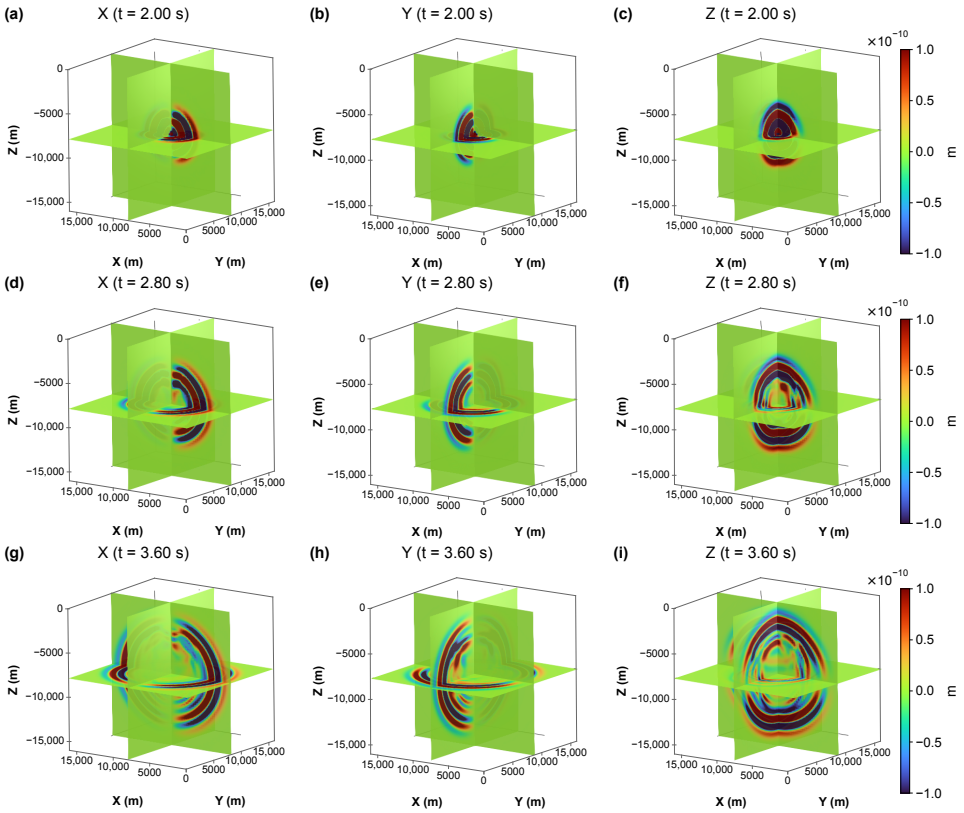


Figure 9. Three-dimensional views of solid displacement in the modified salt-dome model. Columns show u_x, u_y and u_z; rows show $t = 2.00$, 2.80 and 3.60 s, respectively. (**a**) u_x, (**b**) u_y, and (**c**) u_z at 2.00 s; (**d**) u_x, (**e**) u_y, and (**f**) u_z at 2.80 s; (**g**) u_x, (**h**) u_y, and (**i**) u_z at 3.60 s. Each view displays intersecting slices of the three-dimensional field; the vertical axis uses negative elevation below the surface.

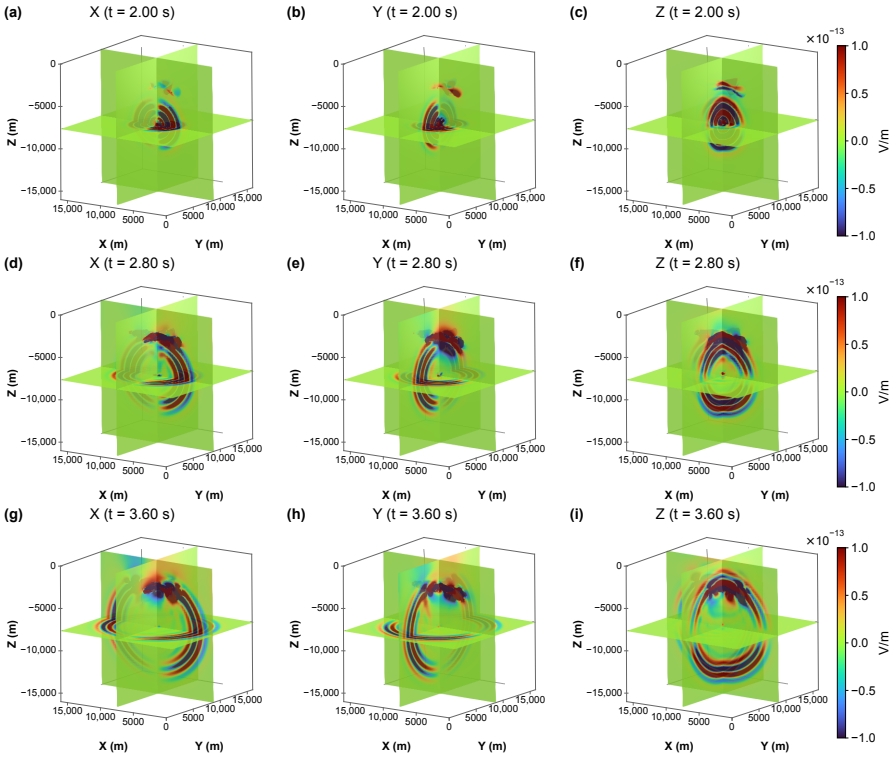


Figure 10. Three-dimensional views of the induced electric field in the modified salt-dome model. Columns show E_x, E_y and E_z; rows show $t = 2.00$, 2.80 and 3.60 s, respectively. (**a**) E_x, (**b**) E_y, and (**c**) E_z at 2.00 s; (**d**) E_x, (**e**) E_y, and (**f**) E_z at 2.80 s; (**g**) E_x, (**h**) E_y, and (**i**) E_z at 3.60 s. Each view displays intersecting slices of the three-dimensional field; the vertical axis uses negative elevation below the surface.

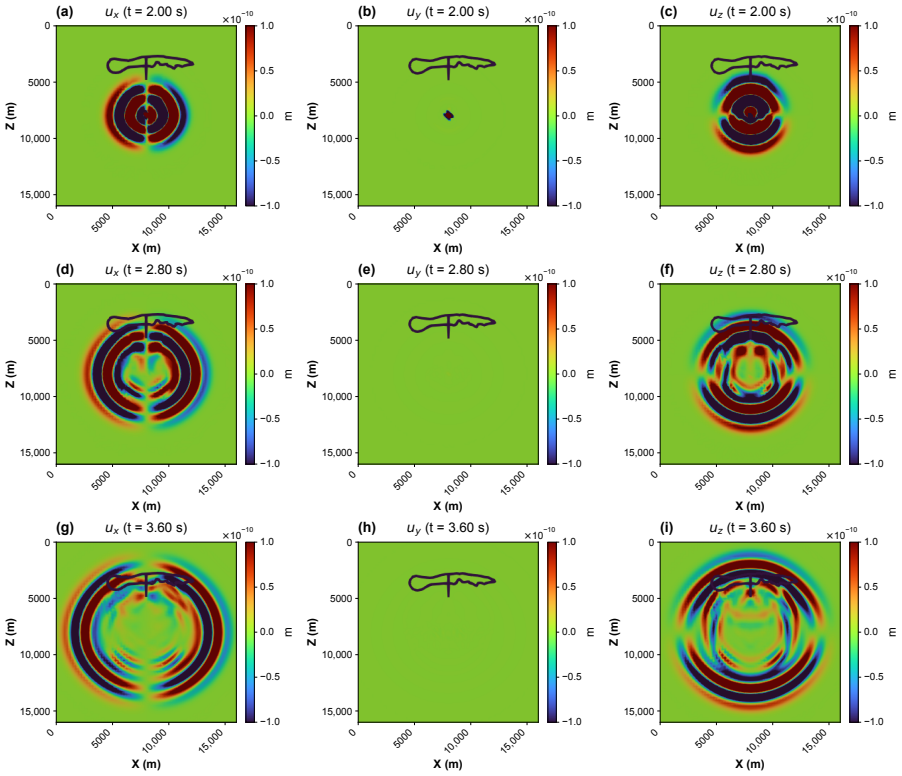


Figure 11. Solid-displacement snapshots in the xz-slice of the modified salt-dome model. Columns show u_x, u_y and u_z; rows show $t = 2.00$, 2.80 and 3.60 s. (**a**) u_x, (**b**) u_y, and (**c**) u_z at 2.00 s; (**d**) u_x, (**e**) u_y, and (**f**) u_z at 2.80 s; (**g**) u_x, (**h**) u_y, and (**i**) u_z at 3.60 s. The black contour shows the intersection of the salt-dome boundary with this section; the vertical coordinate denotes depth.

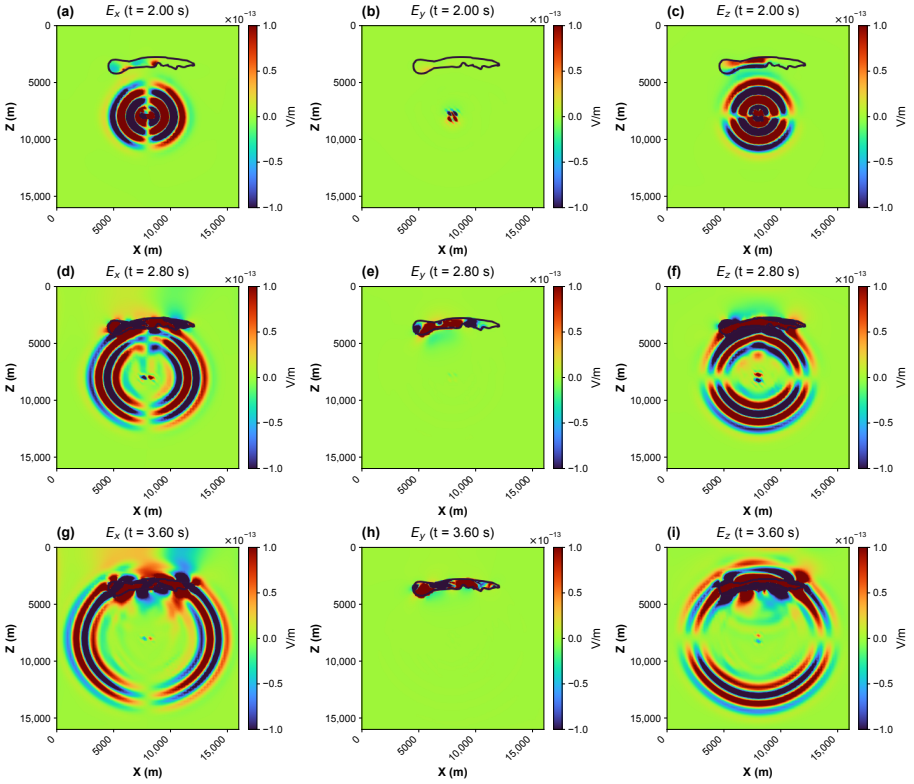


Figure 12. Electric-field snapshots in the xz-slice of the modified salt-dome model. Columns show E_x, E_y and E_z; rows show $t = 2.00$, 2.80 and 3.60 s. (**a**) E_x, (**b**) E_y, and (**c**) E_z at 2.00 s; (**d**) E_x, (**e**) E_y, and (**f**) E_z at 2.80 s; (**g**) E_x, (**h**) E_y, and (**i**) E_z at 3.60 s. The black contour shows the intersection of the salt-dome boundary with this section; the vertical coordinate denotes depth.

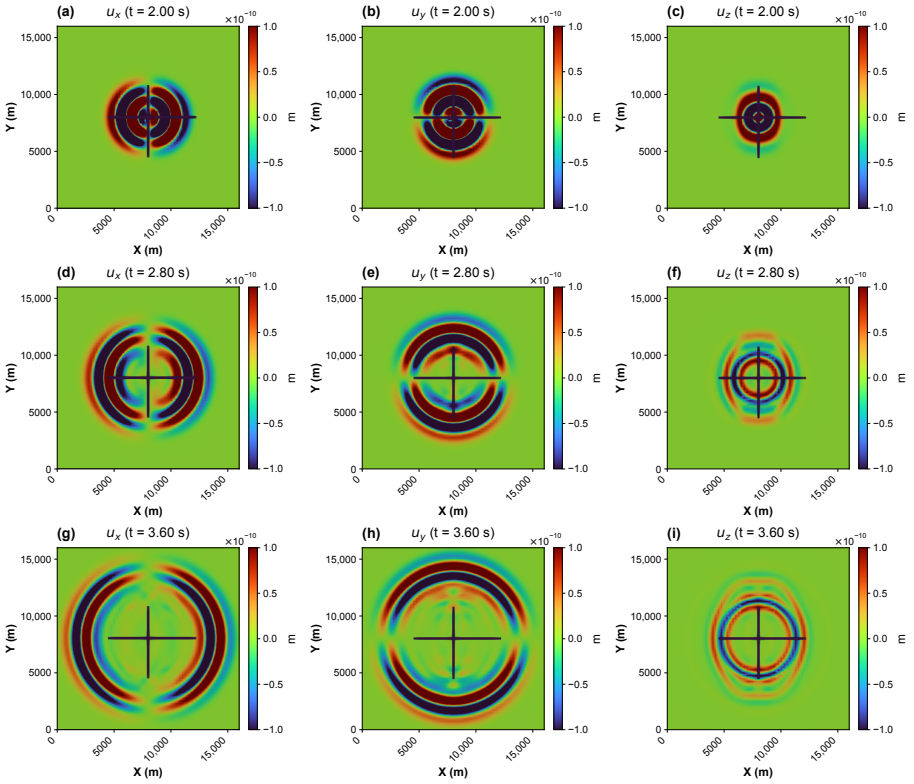


Figure 13. Solid-displacement snapshots in the xy-slice of the modified salt-dome model. Columns show u_x, u_y and u_z; rows show $t = 2.00$, 2.80 and 3.60 s. (**a**) u_x, (**b**) u_y, and (**c**) u_z at 2.00 s; (**d**) u_x, (**e**) u_y, and (**f**) u_z at 2.80 s; (**g**) u_x, (**h**) u_y, and (**i**) u_z at 3.60 s. Horizontal coordinates are in meters.

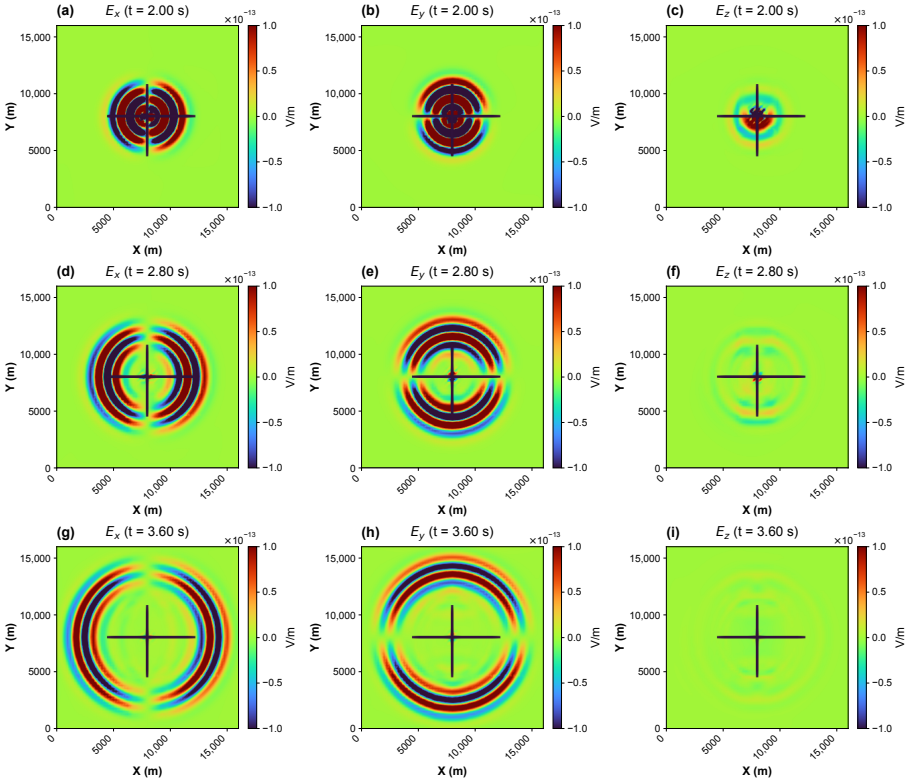


Figure 14. Electric-field snapshots in the xy-slice of the modified salt-dome model. Columns show E_x, E_y and E_z; rows show $t = 2.00$, 2.80 and 3.60 s. (**a**) E_x, (**b**) E_y, and (**c**) E_z at 2.00 s; (**d**) E_x, (**e**) E_y, and (**f**) E_z at 2.80 s; (**g**) E_x, (**h**) E_y, and (**i**) E_z at 3.60 s. Horizontal coordinates are in meters.

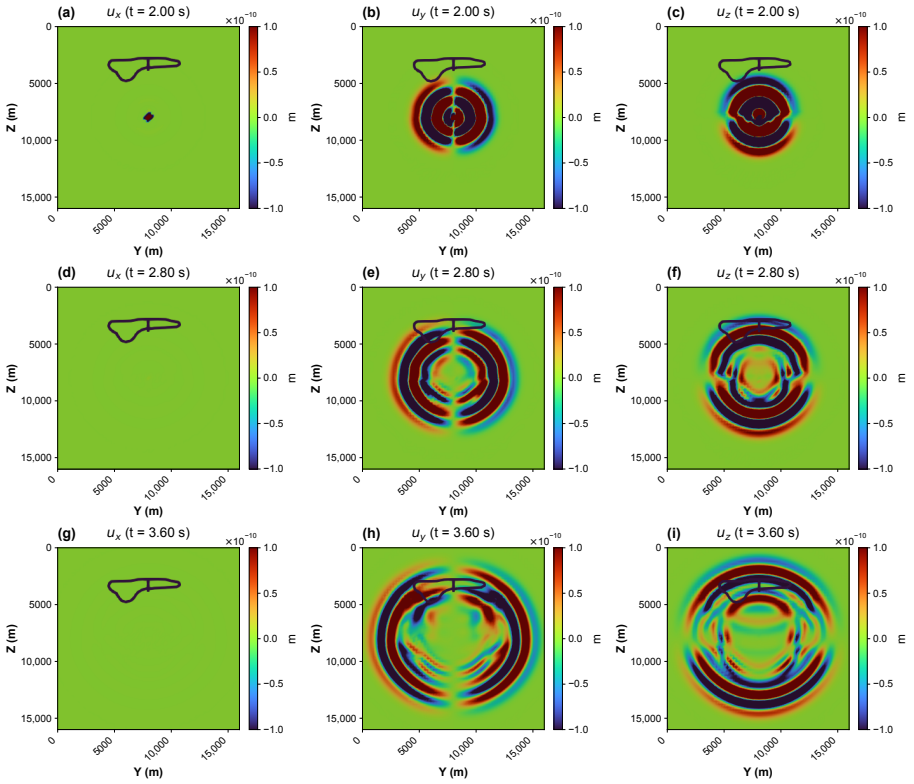


Figure 15. Solid-displacement snapshots in the yz-slice of the modified salt-dome model. Columns show u_x, u_y and u_z; rows show $t = 2.00$, 2.80 and 3.60 s. (**a**) u_x, (**b**) u_y, and (**c**) u_z at 2.00 s; (**d**) u_x, (**e**) u_y, and (**f**) u_z at 2.80 s; (**g**) u_x, (**h**) u_y, and (**i**) u_z at 3.60 s. The black contour shows the intersection of the salt-dome boundary with this section; the vertical coordinate denotes depth.

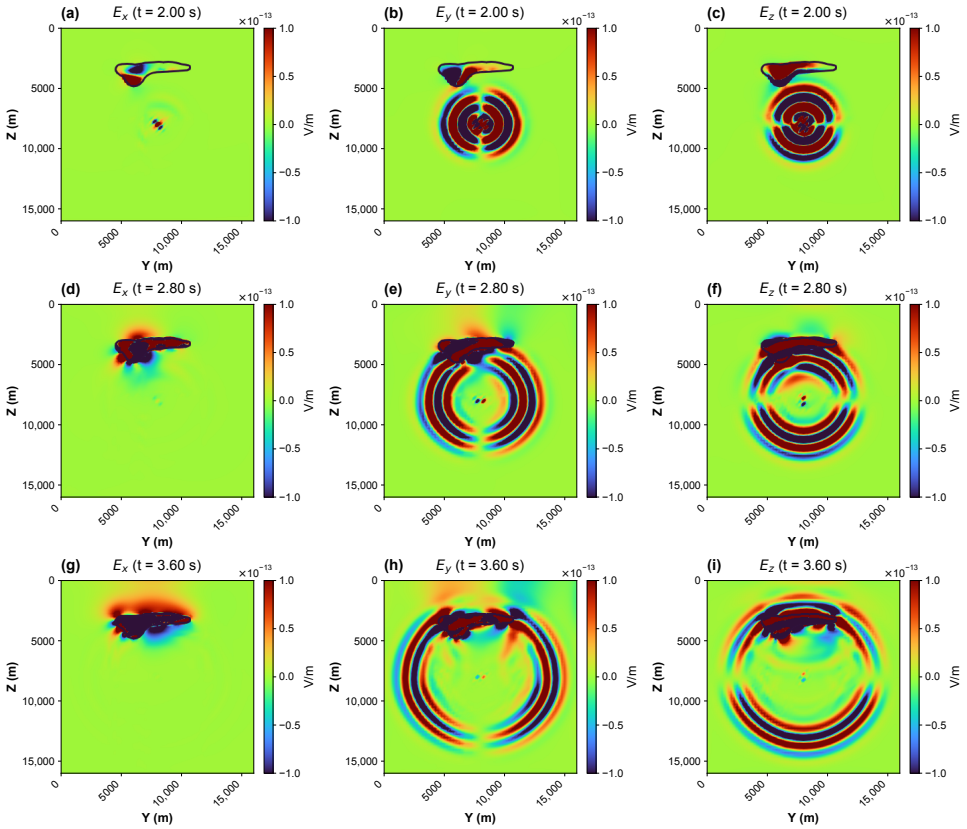


Figure 16. Electric-field snapshots in the yz-slice of the modified salt-dome model. Columns show E_x, E_y and E_z; rows show $t = 2.00$, 2.80 and 3.60 s. (**a**) E_x, (**b**) E_y, and (**c**) E_z at 2.00 s; (**d**) E_x, (**e**) E_y, and (**f**) E_z at 2.80 s; (**g**) E_x, (**h**) E_y, and (**i**) E_z at 3.60 s. The black contour shows the intersection of the salt-dome boundary with this section; the vertical coordinate denotes depth.

To quantify the background anisotropy effect in the same geometry, we compare matched ISO and VTI salt-dome calculations. The ISO background uses $K_b = 5.48$ GPa and $G = 4.95$ GPa, matching the Voigt-averaged moduli of the VTI background; its stiffnesses and the associated Biot coefficients are specified in Appendix D. Inclusion properties, densities, porosities, hydraulic and electromagnetic inputs, source, meshes, boundary conditions and time steps are held fixed. The comparison therefore concerns the background elastic constitutive treatment and its associated poroelastic coupling. Receiver T0 is at (9.5, 9.5) km and a depth of 1 km. Both calculations advance for 6 s, using 0.002 s mechanical and 0.020 s electromagnetic time steps.

Figure 17 shows the three displacement and electric-field components. Table 6 reports the 6 s record differences, using ISO as the reference in the waveform and peak measures of Appendix E. Displacement D_2 values range from 71.71% to 111.12%, whereas electric-field values range from 64.78% to 76.18%. Electric peak magnitudes decrease by 13.58–23.28%. The peak-time differences in the table are measured at the sampled absolute maxima. Except for E_z, all components peak 0.04–0.13 s later, indicating that the VTI background delays the main arrivals slightly; the E_z difference arises because its absolute maximum switches between positive and negative lobes, so it does not correspond to an arrival-time change.

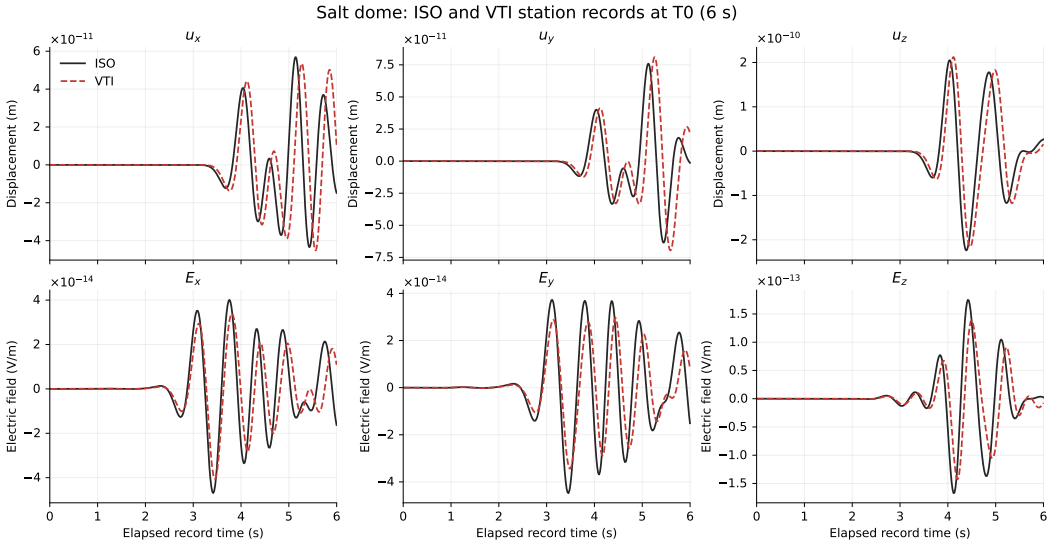


Figure 17. Matched ISO and VTI salt-dome records at T0 over 6 s. Upper row: displacement; lower row: electric field. Black solid: ISO; red dashed: VTI. Columns show the x, y and z components.

Table 6. Salt-dome waveform and peak differences at T0, with ISO as the reference. ΔP is the signed percentage change in absolute peak magnitude; Δt_P is the sampled peak-time shift.

Component	D_2 (%)	ΔP (%)	Δt_P (s)
u_x	111.118	−5.972	+0.128
u_y	110.031	+6.740	+0.132
u_z	71.714	−3.396	+0.080
E_x	64.782	−13.582	+0.040
E_y	64.980	−23.285	+0.040
E_z	76.178	−18.371	−0.220

4. Discussion

The computed results are interpreted in terms of mechanical driving, current generation, and electric-field redistribution at interfaces. These relationships explain how the tool simulates electrokinetic responses for a specified seismic source and geological structure.

The UE comparison changes only the independent stiffness C_{33}^{d} while retaining the reference hydraulic and electromagnetic transport inputs. The electromagnetic response changes through the mechanical driving and relative fluid motion that generate streaming current [1]. The constitutive relations of Cheng [18] link this stiffness change to the Biot coefficients and storage modulus. For U0, $b_h = b_v = 0.250342$ and $M = 9.35570$ GPa; for UE, $b_h = 0.250342$, $b_v = 0.360511$ and $M = 8.93572$ GPa. The elastic perturbation therefore changes the directional poroelastic coupling as well as the restoring force. Estimated locked fluid–frame wave speeds in UE are 2375 m s^{-1} horizontally and 2198 m s^{-1} vertically, compared with 2378 m s^{-1} in U0. These speed estimates are consistent with the directional wavefield differences; the displacement peaks shift by only 0.006–0.008 s, while the later waveforms change markedly.

In UK, the electric field changes despite the small displacement response. With porosity, tortuosity and fluid chemistry fixed and $\Sigma_d = 0$, Equation (A3b) reduces to $\sigma_i = (\phi/T_i)\sigma_f$. Conductivity and permittivity therefore remain unchanged, and permeability affects the electric response through relative fluid motion and current-source conversion. Away from the applied source, the fluid balance along each principal direction is

$$\frac{\rho_f T_i}{\phi}\dot{q}_i + \frac{\eta_f}{k_i}q_i = \mathcal{D}_i, \qquad \mathcal{D}_i = -\partial_i P - \rho_f \ddot{u}_i. \tag{14}$$

Here, q_i is the filtration velocity, and $\mathcal{D}_i$ combines the pressure gradient and frame acceleration. In the viscous limit, the source relation becomes

$$J_{s,i} = L_i \frac{\eta_f}{k_i} q_i \simeq L_i \mathcal{D}_i \quad \text{when fluid inertia is negligible.} \tag{15}$$

For fixed driving, q_i scales with k_i/η_f, offsetting the explicit inverse permeability in the source relation to leading order. In UK, $L_v\eta_f/k_v$ increases by approximately 25%, whereas L_v changes by less than 10^{-4}%. The remaining waveform differences reflect changes in pressure, fluid inertia and the spatial current distribution. Because the electric field responds to a three-dimensional vector source, changing axial permeability also affects the horizontal receiver components.

In UT, axial tortuosity decreases from 3 to 2.4, while the reference elastic properties and permeability remain unchanged. The axial fluid-inertia coefficient decreases by 20%, σ_v increases by 25% and L_v increases by approximately 25%. The axial relative permittivity changes from 9.066667 to 10.333333. These linked changes jointly affect the electric response. The ratio of the coupling coefficient to conductivity is

$$\frac{L_i}{\sigma_i} = -\frac{\varepsilon_0 \varepsilon_{r,f} \zeta}{\eta_f \sigma_f} \left(1 - \frac{2d_D}{\Lambda_i}\right). \tag{16}$$

The explicit tortuosity dependence cancels in this ratio, leaving a small double-layer correction. Under similar mechanical driving and locally conduction-dominated conditions, increased conductivity can offset stronger coupling, helping explain why electric peak magnitudes change by less than 0.64%, while full-record waveform differences reach 1.75–4.97%. Peng et al. [33] examined the influence of tortuosity on the electrokinetic coupling coefficient; the receiver fields considered here also reflect conductivity and fluid motion.

Together, these comparisons show that stiffness affects the electric field through wave propagation and poroelastic coupling, while permeability and tortuosity also regulate relative fluid motion and current generation. For the prescribed 20% parameter reductions, C_{33}^d produces the largest normalized response, and T_v produces a larger electric response than k_v (Table 3). The electric waveforms therefore provide information on hydraulic changes that is less apparent in solid displacement, and their full-record differences capture changes beyond the peak amplitudes alone.

The salt-dome example further demonstrates the framework in a complex three-dimensional model. The simulation shows an electric response accompanying the propagating wavefield and localized electric fields near the inclusion, with some out-of-plane electric components remaining visible where the corresponding displacement components are weak.

5. Conclusions

This study presents a three-dimensional SEM–FETD tool for investigating the contribution of electrokinetic effects to complex seismic electromagnetic signals. Its contribution is the VTI constitutive and transport extension of the existing sequential framework, incorporating directional stiffness, permeability and tortuosity. An explicit poroelastic calculation supplies the filtration velocity for an implicit full-wave electromagnetic solve. The U0 result agrees with the independent reference solution of Hu and Gao [31], and the mesh and time-step check in Section 3.3 indicates convergence of the peak amplitudes at about the 0.2% level for this configuration.

The half-space simulations show that elastic anisotropy changes both seismic waveforms and the associated electric response while electromagnetic transport coefficients remain fixed. Hydraulic perturbations produce weaker displacement changes but appreciable electric differences. Common 20% decreases in C_{33}^d, k_v and T_v give a controlled

finite-change comparison. Permeability and tortuosity perturbations yield displacement differences below 0.16%, with electric differences of 0.97–1.57% and 1.75–4.97%, respectively. These electric differences are well above this convergence level, whereas the displacement differences are not individually resolved. Dividing relative waveform differences by 0.20 provides dimensionless finite-change sensitivities. For this reference model and receiver, the C_{33}^{d} change has the largest response; among the hydraulic changes, T_v has the larger electric response and k_v the larger displacement response. The predicted electric signal thus depends on the mechanical drive and relative fluid motion, together with the coupling and transport properties.

The modified salt-dome simulation demonstrates the method's applicability to an irregular porous inclusion within a VTI background. Approximately elliptical vertical and near-circular horizontal wavefronts are consistent with the directional propagation of the background medium. The different xz- and yz-sections exhibit distinct responses near their salt-dome contours, including localized electric fields and out-of-plane electric components where displacement is weak. These results illustrate the method's ability to represent anisotropic propagation together with spatially complex electrokinetic responses at irregular interfaces. With the same salt-dome geometry, the matched ISO/VTI comparison yields electric-field waveform differences of 64.78–76.18% at T0, quantifying the background elastic constitutive effect in this model. The transport coefficients are evaluated from static Pride relations and the source uses a viscous approximation, so the waveform comparisons and sensitivities apply to the prescribed model under this closure; field application requires site-specific calibration using the source and instrument response, and comparison with observations.

Author Contributions: Conceptualization, P.L. and Z.A.; methodology, P.L., Z.A., Y.F., Y.L. and Y.H.; software, P.L. and X.C.; validation, Y.F. and Y.L.; formal analysis, P.L., Y.L., X.C. and Y.H.; investigation, P.L. and Y.H.; resources, Y.F. and Y.L.; data curation, Z.A., Y.F. and X.C.; writing—original draft preparation, P.L.; writing—review and editing, P.L.; visualization, X.C. and Y.H.; supervision, Z.A. and Y.H.; project administration, P.L. and Z.A.; funding acquisition, Z.A. and Y.F. All authors have read and agreed to the published version of the manuscript.

Funding: This work was supported by the Spark Program of Earthquake Sciences (Grant No. XH24045A), the Central Public-interest Scientific Institution Basal Research Fund (Grant No. LISCEA202509), and the National Natural Science Foundation of China (NSFC) (Grant No. 41374080).

Institutional Review Board Statement: Not applicable.

Informed Consent Statement: Not applicable.

Data Availability Statement: To enhance reproducibility, the waveform datasets and model configuration files are publicly available in the Zenodo repository at https://doi.org/10.5281/zenodo.23292028 (accessed on 4 November 2026). The core solver software may be shared upon reasonable request to the corresponding author, subject to institutional restrictions.

Acknowledgments: The authors acknowledge the support of the Spark Program of Earthquake Sciences and NSFC.

Conflicts of Interest: The authors declare no conflicts of interest.

Abbreviations

VTI	Vertical transverse isotropy
SEM	Spectral-element method
FETD	Finite-element time-domain method
GLL	Gauss–Lobatto–Legendre
PML	Perfectly matched layer

CFL	Courant–Friedrichs–Lewy
MUMPS	MUltifrontal Massively Parallel sparse direct Solver
SEG	Society of Exploration Geophysicists
EAEG	European Association of Exploration Geophysicists

Appendix A. VTI Constitutive Coefficients and Model Limits

We exclude partial saturation, induced polarization, grain-interior conduction and Stern-layer conduction from the material model.

For horizontal and vertical directions, denoted by h and v, the permeability and tortuosity tensors are

$$\mathbf{K} = \mathrm{diag}(k_h, k_h, k_v), \qquad \mathbf{T}_\infty = \mathrm{diag}(T_h, T_h, T_v). \tag{A1}$$

The drained elastic response is specified by five independent VTI stiffnesses. In Voigt notation, $\mathbf{C}^d$ and $\mathbf{C}^u$ denote the drained and undrained stiffness matrices, respectively. The directional Biot coefficients form $\mathbf{b}_V = (b_h, b_h, b_v, 0, 0, 0)^T$, and M is the fluid-storage modulus. We calculated these coefficients using the relations derived by Cheng [18], given below.

The electrokinetic coupling, conductivity, and permittivity have the same principal directions:

$$\begin{aligned} \mathbf{L} &= \mathrm{diag}(L_h, L_h, L_v), \\ \boldsymbol{\sigma} &= \mathrm{diag}(\sigma_h, \sigma_h, \sigma_v), \\ \boldsymbol{\varepsilon} &= \mathrm{diag}(\varepsilon_h, \varepsilon_h, \varepsilon_v). \end{aligned} \tag{A2}$$

Pride [1] derived the isotropic electrokinetic transport relations, whose static limits are also presented by Grobbe and Slob [34]. We apply those limits separately along each principal direction as an effective closure for thin electrical double layers. The diagonal tensor structure follows the assumed VTI symmetry, whereas applying the scalar coefficient relations along each principal direction is an effective material closure. Pride's derivation relates the electrical formation factor to the geometric tortuosity that also enters the inertial term; extending this relation to each principal direction is part of the closure adopted here. Tortuosity measures associated with different transport processes need not coincide in anisotropic media [33], so this identification remains an additional modeling assumption. With $F_i = T_i/\phi$, $i \in \{h, v\}$, the directional coefficients are

$$L_i = -\frac{\varepsilon_0 \varepsilon_{r,f} \zeta}{\eta_f F_i}\left(1 - \frac{2d_D}{\Lambda_i}\right), \tag{A3a}$$

$$\sigma_i = \frac{1}{F_i}\left(\sigma_f + \frac{2\Sigma_d}{\Lambda_i}\right), \tag{A3b}$$

$$\varepsilon_i = \varepsilon_0\left[\varepsilon_{r,s} + \frac{\varepsilon_{r,f} - \varepsilon_{r,s}}{F_i}\right]. \tag{A3c}$$

Here, η_f is fluid viscosity, σ_f is fluid conductivity, ε_0 is vacuum permittivity, and $\varepsilon_{r,f}$ and $\varepsilon_{r,s}$ are the relative permittivities of fluid and grains. The remaining parameters are the zeta potential ζ, Debye length d_D, directional pore length Λ_i, and diffuse-layer excess conductance Σ_d. We apply the isotropic effective-permittivity relation summarized by Wapenaar [35] along each principal direction. The pore-length closure and thin-double-layer condition are given below.

The Voigt stress and engineering-strain vectors are

$$\begin{aligned} \boldsymbol{\tau}_V &= (\tau_{xx}, \tau_{yy}, \tau_{zz}, \tau_{yz}, \tau_{xz}, \tau_{xy})^T, \\ \mathbf{e}_V &= (e_{xx}, e_{yy}, e_{zz}, 2e_{yz}, 2e_{xz}, 2e_{xy})^T, \end{aligned} \tag{A4}$$

where $\mathbf{e} = \frac{1}{2}[\nabla\mathbf{u} + (\nabla\mathbf{u})^T]$. The drained stiffness matrix is

$$\mathbf{C}^d = \begin{bmatrix} C_{11}^d & C_{12}^d & C_{13}^d & 0 & 0 & 0 \\ C_{12}^d & C_{11}^d & C_{13}^d & 0 & 0 & 0 \\ C_{13}^d & C_{13}^d & C_{33}^d & 0 & 0 & 0 \\ 0 & 0 & 0 & C_{44}^d & 0 & 0 \\ 0 & 0 & 0 & 0 & C_{44}^d & 0 \\ 0 & 0 & 0 & 0 & 0 & C_{66}^d \end{bmatrix}, \qquad C_{12}^d = C_{11}^d - 2C_{66}^d. \tag{A5}$$

For microhomogeneous isotropic grains, the Biot coefficients and storage modulus are [18]

$$\begin{aligned} b_h &= 1 - \frac{C_{11}^d + C_{12}^d + C_{13}^d}{3K_s}, \\ b_v &= 1 - \frac{2C_{13}^d + C_{33}^d}{3K_s}, \\ M^{-1} &= \frac{\phi}{K_f} + \frac{(2b_h + b_v)/3 - \phi}{K_s}, \end{aligned} \tag{A6}$$

where K_s and K_f are the grain and fluid bulk moduli. Eliminating pore pressure gives the undrained stiffness used in Equation (A8):

$$\mathbf{C}^u = \mathbf{C}^d + M\mathbf{b}_V\mathbf{b}_V^T. \tag{A7}$$

These coefficients enter the stress and pore-pressure relations

$$\boldsymbol{\tau}_V = \mathbf{C}^u\mathbf{e}_V + M\mathbf{b}_V\nabla\cdot\mathbf{w}, \tag{A8}$$

$$-P = M\left[b_h\left(\frac{\partial u_x}{\partial x} + \frac{\partial u_y}{\partial y}\right) + b_v\frac{\partial u_z}{\partial z}\right] + M\nabla\cdot\mathbf{w}, \tag{A9}$$

The undrained-stiffness update changes the normal-stress coefficients and leaves the shear stiffnesses unchanged. Admissible inputs satisfy positive-definite $\mathbf{C}^d$, $M > 0$, $0 < \phi < 1$, $k_i > 0$, and $T_i \geq 1$.

The pore lengths in Equation (A3) may be specified independently or related to permeability and tortuosity through

$$\Lambda_i = \left(\frac{m_0 T_i k_i}{\phi}\right)^{1/2}, \qquad i \in \{h, v\}, \tag{A10}$$

where m_0 is a prescribed dimensionless pore-shape parameter. This is an additional geometric closure. The electrokinetic relation assumes $d_D/\Lambda_i \ll 1$. The excess conductance Σ_d includes diffuse-layer electromigration and electroosmotic contributions; setting $\Sigma_d = 0$ neglects these contributions to conductivity. Fluid and double-layer parameters are prescribed from fluid chemistry and temperature.

The low-frequency and weak-feedback conditions are expressed using

$$f_{c,i} = \frac{\phi\eta_f}{2\pi\rho_f T_i k_i}, \qquad \chi_i = \frac{\eta_f L_i^2}{k_i\sigma_i}. \tag{A11}$$

The viscous source conversion is asymptotically justified when $f/f_{c,i} \ll 1$, while neglecting electroosmotic feedback requires $\chi_i \ll 1$. These are distinct criteria. The finite frequency ratios for the present inputs are given in Appendix B. For the solid-frame source used here, $\mathbf{f}_f = 0$. The fluid momentum balance retains inertia and relates the mechanical driving force to both viscous and inertial contributions. Using the complete driving force with the same static coupling tensor gives

$$\begin{aligned} \mathbf{J}_s^{(\mathrm{drive})} &= \mathbf{L}\left(-\nabla P - \rho_f\ddot{\mathbf{u}}\right), \\ \mathbf{J}_s^{(\mathrm{drive})} - \mathbf{J}_s^{(\mathrm{vis})} &= \frac{\rho_f}{\phi}\mathbf{L}\mathbf{T}_\infty\frac{\partial\mathbf{q}}{\partial t}, \end{aligned} \tag{A12}$$

where $\mathbf{J}_s^{(\mathrm{vis})} = \eta_f \mathbf{L}\mathbf{K}^{-1}\mathbf{q}$ is the source used in the reported simulations. This identity follows from Equation (2) and the adopted static transport relation [1,10]. It identifies a source-conversion approximation, even though fluid inertia is retained in the mechanical solve. The ratio of the omitted term to the viscous term for a harmonic component scales as $f/f_{c,i}$; it is not a bound on the receiver electric-field error. The driving-force expression still uses static coefficients and neglects electroosmotic feedback. These hydraulic approximations do not remove electromagnetic displacement current.

The ratio L_i/σ_i in Equation (16) is independent of the formation factor F_i at fixed fluid chemistry and pore length. A change in this factor scales the streaming-current source and conductivity proportionally. In the conduction-dominated limit, the balance $\nabla \cdot (\boldsymbol{\sigma} \nabla \varphi) = \nabla \cdot \mathbf{J}_s$ is invariant under a common rescaling of both quantities. This provides a leading-order analytical explanation for compensation between source and conductivity changes; permittivity and frequency-dependent transport lie outside this argument.

For the isotropic limit, set $k_h = k_v = k$, $T_h = T_v = T_\infty$, $\Lambda_h = \Lambda_v$, and

$$\begin{aligned} C_{11}^d &= C_{33}^d = K_b + \frac{4}{3}G, \\ C_{12}^d &= C_{13}^d = K_b - \frac{2}{3}G, \\ C_{44}^d &= C_{66}^d = G. \end{aligned} \tag{A13}$$

Here, K_b and G are the drained bulk and shear moduli. Then $b_h = b_v = \alpha = 1 - K_b/K_s$, $C_{11}^u = C_{33}^u = H$, and $C_{12}^u = C_{13}^u = H - 2G$, with $H = K_b + 4G/3 + \alpha^2 M$. The transport tensors become scalar coefficients, recovering the isotropic formulation.

Appendix B. Reference Fluid and Electrochemical Parameters

Table A1. Reference properties for the half-space simulations. K_b and G are drained frame moduli.

Quantity	Value	Quantity	Value
ρ_s (kg m^{-3})	2550	ρ_f (kg m^{-3})	1000
ϕ	0.20	η_f (Pa s)	10^{-3}
K_s (GPa)	7.31	K_f (GPa)	2.00
K_b (GPa)	5.48	G (GPa)	4.95
k_0 (m^2)	10^{-9}	T_0	3
$\varepsilon_{r,s}$	4	$\varepsilon_{r,f}$	80
C_f (mol L^{-1})	0.082	T_{ref} (K)	293.15

We calculated the electromagnetic coefficients from Equation (A3), using the fluid relations below. We set $\Sigma_d = 0$ to omit surface conduction while retaining electrokinetic coupling. For U0 and UE, effective conductivity is 0.0536463 S m^{-1}, coupling is 9.55814×10^{-10} s C kg^{-1}, and relative permittivity is 9.066667 in each direction. UK retains the conductivity and permittivity, with a small pore-length correction to axial coupling. UT changes axial conductivity, coupling and relative permittivity to 0.0670579 S m^{-1}, 1.19477×10^{-9} s C kg^{-1} and 10.333333, respectively. Its transverse coefficients remain unchanged. Absolute permittivity is ε_0 times relative permittivity.

We used aqueous NaCl at $T_{\mathrm{ref}} = 293.15$ K as the reference electrolyte and prescribe fluid density, viscosity, bulk modulus and relative permittivity as approximate constants. Their salinity dependence is neglected over the concentration range considered here, whereas fluid conductivity and electrochemical parameters are evaluated separately for each material.

To distinguish molarity from molality, define the dimensionless quantities

$$c_f = \frac{C_f}{1\,\mathrm{mol\,L^{-1}}}, \qquad r_f = \frac{\rho_f}{1000\,\mathrm{kg\,m^{-3}}}, \qquad \widehat{m}_f = \frac{m_f}{1\,\mathrm{mol\,kg^{-1}}}. \tag{A14}$$

Using the rounded NaCl molar mass adopted in the material inputs, $M_{\mathrm{NaCl}} = 0.05844\,\mathrm{kg\,mol^{-1}}$, the concentration conversion is

$$\widehat{m}_f = \frac{c_f}{r_f - 0.05844 c_f}. \tag{A15}$$

The denominator accounts for the solvent mass in one liter of solution under the prescribed density approximation.

We calculated pore-fluid conductivity with the empirical relation of Sen and Goode [36], also used by Aoyama and Hashimoto [37]:

$$\frac{\sigma_f}{1\,\mathrm{S\,m^{-1}}} = \left(5.6 + 0.27\vartheta - 1.5\times10^{-4}\vartheta^2\right)\widehat{m}_f - \frac{(2.36 + 0.099\vartheta)\widehat{m}_f^{3/2}}{1 + 0.214\widehat{m}_f^{1/2}}, \tag{A16}$$

where ϑ is the numerical temperature in degrees Celsius, set to 20 in these simulations.

We used the empirical zeta-potential relation of Pride and Morgan [38], as adopted by Wang et al. [39]:

$$\frac{\zeta}{1\,\mathrm{V}} = 0.008 + 0.026\log_{10}(c_f). \tag{A17}$$

We use this quartz-like pore-surface relation as a constitutive input for the synthetic materials.

For a symmetric monovalent electrolyte, the Debye length is

$$d_D = \left(\frac{\varepsilon_0\varepsilon_{r,f}k_BT_{\mathrm{ref}}}{2e^2N_Ac_m}\right)^{1/2}, \qquad c_m = 1000c_f\,\mathrm{mol\,m^{-3}}, \tag{A18}$$

where k_B, e, and N_A are the Boltzmann constant, elementary charge, and Avogadro constant, respectively.

The pore-shape parameter in Equation (A10) is set to $m_0 = 8$ as a capillary-based geometric reference for these models. The relation is applied separately in the horizontal and vertical directions as an effective geometric assumption. The fluid conductivity, zeta potential, and Debye length are scalar within each material. Directional electrokinetic and electromagnetic coefficients were calculated using Equation (A3).

We omitted surface conduction by setting $\Sigma_d = 0$. For a scale estimate, we used the quartz specific surface conductance 8.9×10^{-9} S reported by Revil and Glover [40] at 25 °C and salinities above $10^{-3}\,\mathrm{mol\,L^{-1}}$. This reference value gives a maximum $2\Sigma_s/(\sigma_f\Lambda_i)$ of approximately 7.14×10^{-5} for the homogeneous parameter cases. This supports bulk-fluid-dominated conduction for those prescribed inputs. The reference Σ_s is used only for this estimate and is not assigned as the diffuse-layer coefficient Σ_d.

For the homogeneous material configurations in Section 3.1,

$$\max_i\left(\frac{d_D}{\Lambda_i}\right) \approx 3.43\times10^{-6}, \qquad \max_i\chi_i \approx 2.13\times10^{-11}. \tag{A19}$$

The maxima also extend over the homogeneous comparison cases. These values support the thin-double-layer and weak-feedback assumptions, independently of the hydraulic frequency criterion.

For U0 and UE, the hydraulic characteristic frequency is 10.6103 Hz; the axial value in UK and UT is 13.2629 Hz. The largest $f/f_{c,i}$ is approximately 0.0942 at 1 Hz and 0.283 at

3 Hz. The latter is a representative frequency for a scale comparison, rather than a strict spectral cutoff for the Ricker source. The viscous source approximation therefore has finite inertial corrections described by Equation (A12). This hydraulic criterion is separate from retaining electromagnetic displacement current.

Appendix C. Time Discretization and Finite-Element Assembly

The constitutive relations $\mathbf{D} = \boldsymbol{\varepsilon}\mathbf{E}$ and $\mathbf{B} = \mu_0\mathbf{H}$ accompany Gauss's laws $\nabla \cdot \mathbf{D} = \rho_e$ and $\nabla \cdot \mathbf{B} = 0$, where ρ_e is free-charge density. Taking the divergence of Equation (3) gives total-current continuity:

$$\nabla \cdot \left(\boldsymbol{\sigma}\mathbf{E} + \boldsymbol{\varepsilon}\frac{\partial \mathbf{E}}{\partial t} + \mathbf{J}_s \right) = 0. \tag{A20}$$

For constant magnetic permeability, the gauge-regularized operator is

$$\mathcal{L}_g\mathbf{A} = \nabla \times (\mu_0^{-1}\nabla \times \mathbf{A}) - \nabla(\mu_0^{-1}\nabla \cdot \mathbf{A}). \tag{A21}$$

The grad–div term vanishes for a Coulomb-gauge solution.

Bíró and Preis [41] discussed magnetic-vector-potential finite-element formulations for three-dimensional eddy-current problems. Here, we chose the Coulomb gauge and added a grad–div regularization to our full-wave potential equations. Substitution of Equation (6) into Ampere's law gives

$$\mathcal{L}_g\mathbf{A} + \boldsymbol{\sigma}\frac{\partial \mathbf{A}}{\partial t} + \boldsymbol{\varepsilon}\frac{\partial^2 \mathbf{A}}{\partial t^2} + \boldsymbol{\sigma}\nabla\varphi + \boldsymbol{\varepsilon}\nabla\frac{\partial \varphi}{\partial t} = \mathbf{J}_s, \tag{A22}$$

The scalar-potential equation follows from total-current continuity. Conductivity and permittivity remain tensors within the operators.

At t_{n+1}, the time derivatives are approximated using

$$\begin{aligned} \left.\frac{\partial \xi}{\partial t}\right|_{t_{n+1}} &\approx \frac{\xi^{n+1} - \xi^n}{\Delta t}, \\ \left.\frac{\partial^2 \mathbf{A}}{\partial t^2}\right|_{t_{n+1}} &\approx \frac{\mathbf{A}^{n+1} - 2\mathbf{A}^n + \mathbf{A}^{n-1}}{\Delta t^2}, \end{aligned} \tag{A23}$$

where ξ denotes either potential or a vector-potential component. Both approximations are first-order accurate at t_{n+1}. Define

$$\mathbf{Q} = \boldsymbol{\sigma} + \frac{\boldsymbol{\varepsilon}}{\Delta t}, \qquad \mathbf{W} = \frac{\mathbf{Q}}{\Delta t}, \tag{A24}$$

and

$$\mathbf{h}^n = \left(\frac{\boldsymbol{\sigma}}{\Delta t} + \frac{2\boldsymbol{\varepsilon}}{\Delta t^2} \right)\mathbf{A}^n - \frac{\boldsymbol{\varepsilon}}{\Delta t^2}\mathbf{A}^{n-1} + \frac{\boldsymbol{\varepsilon}}{\Delta t}\nabla\varphi^n. \tag{A25}$$

The source and history fields enter through $\mathbf{g}^{n+1} = \mathbf{J}_s^{n+1} + \mathbf{h}^n$.

For vector and scalar test functions $\mathbf{v}$ and ψ, define the physical-domain bilinear form

$$a_g(\mathbf{v}, \mathbf{A}) = \int_{\Omega_e} \mu_0^{-1}[(\nabla \times \mathbf{v}) \cdot (\nabla \times \mathbf{A}) + (\nabla \cdot \mathbf{v})(\nabla \cdot \mathbf{A})]\, \mathrm{d}\Omega. \tag{A26}$$

The weak Equations are

$$a_g(\mathbf{v}, \mathbf{A}^{n+1}) + \int_{\Omega_e} \mathbf{v} \cdot \left(\mathbf{W}\mathbf{A}^{n+1} + \mathbf{Q}\nabla\varphi^{n+1} \right) \mathrm{d}\Omega = \int_{\Omega_e} \mathbf{v} \cdot \mathbf{g}^{n+1}\, \mathrm{d}\Omega, \tag{A27a}$$

$$\int_{\Omega_e} \nabla\psi \cdot \left(\mathbf{W}\mathbf{A}^{n+1} + \mathbf{Q}\nabla\varphi^{n+1} \right) \mathrm{d}\Omega = \int_{\Omega_e} \nabla\psi \cdot \mathbf{g}^{n+1}\, \mathrm{d}\Omega. \tag{A27b}$$

Let N_a be scalar nodal shape functions and $\mathbf{V}_{ai} = N_a \mathbf{e}_i$, where $\mathbf{e}_i$ is a Cartesian unit vector. With $\mathbf{A}_h = \sum_{a,i} \mathbf{V}_{ai} a_{ai}$ and $\varphi_h = \sum_a N_a \varphi_a$, the assembled block entries are

$$\begin{aligned}
(\mathbf{K}_{AA})_{ai,bj} &= a_g(\mathbf{V}_{ai}, \mathbf{V}_{bj}) + \int_{\Omega_e} \mathbf{V}_{ai} \cdot \mathbf{W}\mathbf{V}_{bj} \, \mathrm{d}\Omega, \\
(\mathbf{K}_{A\varphi})_{ai,b} &= \int_{\Omega_e} \mathbf{V}_{ai} \cdot \mathbf{Q}\nabla N_b \, \mathrm{d}\Omega, \\
(\mathbf{K}_{\varphi A})_{a,bj} &= \int_{\Omega_e} \nabla N_a \cdot \mathbf{W}\mathbf{V}_{bj} \, \mathrm{d}\Omega, \\
(\mathbf{K}_{\varphi\varphi})_{a,b} &= \int_{\Omega_e} \nabla N_a \cdot \mathbf{Q}\nabla N_b \, \mathrm{d}\Omega.
\end{aligned} \tag{A28}$$

The assembled equations take the block form

$$\begin{bmatrix} \mathbf{K}_{AA} & \mathbf{K}_{A\varphi} \\ \mathbf{K}_{\varphi A} & \mathbf{K}_{\varphi\varphi} \end{bmatrix} \begin{bmatrix} \mathbf{a}^{n+1} \\ \boldsymbol{\varphi}^{n+1} \end{bmatrix} = \begin{bmatrix} \mathbf{r}_A^n \\ \mathbf{r}_\varphi^n \end{bmatrix} + \begin{bmatrix} \mathbf{s}_A^{n+1} \\ \mathbf{s}_\varphi^{n+1} \end{bmatrix}. \tag{A29}$$

Here, $\mathbf{a}$ and $\boldsymbol{\varphi}$ collect the nodal potentials, $\mathbf{r}$ contains the previous-time contributions, and $\mathbf{s}$ contains the streaming-current source. The vectors $\mathbf{r}_A$ and $\mathbf{r}_\varphi$ are obtained by testing $\mathbf{h}^n$ with $\mathbf{V}_{ai}$ and ∇N_a, respectively. The source vectors use the same integrals with $\mathbf{J}_s^{n+1}$ in place of $\mathbf{h}^n$.

These expressions describe the physical domain. In the PML, the corresponding transformed operators, integration weights, and history terms are included consistently in both potential equations. At the outer termination, $\mathbf{n}\times\mathbf{A} = \mathbf{0}$ and $\varphi = 0$ are imposed, together with the compatible natural gauge condition $\nabla \cdot \mathbf{A} = 0$. Before coordinate transformation, the divergence of the vector equation and total-current continuity give a homogeneous Laplace equation for $\nabla \cdot \mathbf{A}$; the gauge boundary condition selects its zero solution. Zero initial fields are represented by $\mathbf{A}^{-1} = \mathbf{A}^0 = \mathbf{0}$ and $\varphi^0 = 0$.

We initialized the calculation from rest with zero electromagnetic fields and imposed a traction-free, hydraulically open ground surface, $\boldsymbol{\tau}\mathbf{n} = \mathbf{0}$ and $P = 0$. At welded, hydraulically connected porous interfaces, solid displacement, traction, pore pressure, and normal filtration velocity are continuous. Lateral and bottom seismic boundaries use the first-order paraxial absorbing conditions of Clayton and Engquist [29]. Their approximate treatment of oblique and anisotropic arrivals requires adequate separation between the truncation boundaries and the region of interest.

We treat the air–earth boundary as a material interface. In the absence of imposed sheet currents, tangential electric and magnetic fields, normal magnetic induction, and normal total current are continuous. Normal electric displacement may jump because of interfacial charge. The electromagnetic PML is applied consistently to the anisotropic potential equations. Its outer termination and gauge conditions are given above.

Seismic resolution requirements are set by the shortest relevant directional wavelengths and the pressure and flow gradients associated with the slow compressional mode. The explicit time step is constrained by the Courant–Friedrichs–Lewy (CFL) condition based on the maximum directional wave speed and minimum Gauss–Lobatto–Legendre node spacing, together with the stability requirement of the viscous update. Electromagnetic resolution must account for material interfaces and field variation; the implicit time step was selected for temporal accuracy and source-bandwidth resolution. Spatial and temporal refinement and boundary separation determine the numerical accuracy of these calculations.

Appendix D. Salt-Dome Material Configuration

The modified salt-dome simulation in Section 3.4 extends the controlled half-space comparisons to heterogeneous media. It comprises a VTI porous background surrounding an isotropic porous inclusion, with the background symmetry axis parallel to global z. We

assign synthetic porous-medium properties to the inclusion. Table A2 lists the material inputs. The domain dimensions, source position and inclusion geometry are given in Section 3.4 and Figure 8.

Table A2. Material inputs for the modified salt-dome simulation. Stiffnesses are drained coefficients; transport is locally isotropic in each material.

Parameter	Background	Porous Inclusion
ρ_s (kg m^{-3})	2550	2400
ρ_f (kg m^{-3})	1000	980
ϕ	0.2	0.4
K_s (GPa)	7.31	4.69
K_f (GPa)	2.00	2.25
K_b (GPa)	5.48	1.06
G (GPa)	4.95	5.94
C^d_{11} (GPa)	12.948895	8.980000
C^d_{33} (GPa)	10.790746	8.980000
C^d_{44} (GPa)	4.432040	5.940000
C^d_{66} (GPa)	5.761652	5.940000
C^d_{13} (GPa)	2.445071	−2.900000
$T_h = T_v$	3	3
$k_h = k_v$ (m^2)	10^{-9}	10^{-9}
η_f (Pa s)	10^{-3}	10^{-3}
C_f (mol L^{-1})	0.082	0.00082
$\sigma_h = \sigma_v$ (S m^{-1})	0.0536463	0.00120666
$L_h = L_v$ (s C kg^{-1})	9.55814×10^{-10}	6.82217×10^{-9}
$\varepsilon_{r,h} = \varepsilon_{r,v}$	9.066667	14.133333

We used a reference temperature of 293.15 K and constituent relative permittivities of four and 80. We set $\Sigma_d = 0$ and specify the coupling coefficient separately for each material using its fluid salinity. The salt-dome background retained the fixed stiffnesses in Table A2. The inclusion satisfies the isotropic relations, including $C^d_{13} = K_b - 2G/3 = -2.90$ GPa; its negative coupling entry is compatible with positive-definite stiffness.

We used a 1 Hz Ricker source, a 0.002 s time increment and a 250 m reference element size. The mechanical and electromagnetic material identifiers are 1 for the background and 2 for the inclusion; the electromagnetic air region uses identifier 9.

For the matched ISO reference in Figure 17, the background stiffnesses are $C^d_{11} = C^d_{33} = 12.08$ GPa, $C^d_{12} = C^d_{13} = 2.18$ GPa and $C^d_{44} = C^d_{66} = 4.95$ GPa. They preserve the VTI background's Voigt-averaged K_b and G to the precision of the listed inputs. The ISO Biot coefficients are $b_h = b_v = 0.250342$, compared with $b_h = 0.233034$ and $b_v = 0.284957$ in VTI; both have $M \approx 9.35570$ GPa. The porous inclusion and transport coefficients are unchanged.

Appendix E. Waveform Sampling and Comparison Measures

The matched salt-dome comparison used 3000 displacement samples and 300 electric-field samples over a configured 6 s calculation. Displacement elapsed time is the native SEMD time minus its first sample, spanning 0–5.998 s; electric elapsed time is $(n_{\text{saved}} - 1) \times 0.002$ s, spanning 0.018–5.998 s. The stored component signs and physical amplitudes were retained. ISO is the reference for D_2, peak magnitude and sampled peak-time differences.

The controlled U0, UE, UK and UT comparisons used 3500 displacement samples at 0.002 s intervals and 350 electric-field samples at 0.020 s intervals. Displacement records have native times from approximately −1.200 to 5.798 s and are displayed as elapsed record time $t_u = t_{\text{native}} - t_{\text{native},0}$, spanning approximately 0–6.998 s. Electric display time is the

saved mechanical step index multiplied by 0.002 s, spanning 0.02–7.00 s. This corresponds to an electromagnetic solve and output interval of 0.020 s, with one electromagnetic update per ten mechanical steps.

Windowed D_2 uses the reference norm within that window. The signed residual is

$$\delta a^{(m)}(t) = 100\frac{a^{(m)}(t) - a^{(\mathrm{ref})}(t)}{\max_t |a^{(\mathrm{ref})}(t)|}. \tag{A30}$$

The peak measures are

$$P_a^{(m)} = \max_t |a^{(m)}(t)|, \qquad \Delta P_a^{(m)} = 100\left(\frac{P_a^{(m)}}{P_a^{(\mathrm{ref})}} - 1\right), \qquad \Delta t_{P,a}^{(m)} = t_{P,a}^{(m)} - t_{P,a}^{(\mathrm{ref})}. \tag{A31}$$

The sampled peak time identifies the largest absolute lobe and is not a first-arrival pick. The U0 displacement peaks in x, y and z are 3.77948, 3.77989 and 3.78243 × 10^{-10} m, respectively, where the 10^{-10} factor applies to all three values. The electric peaks are 3.18765, 3.18738 and 3.34746 × 10^{-13} V m^{-1}, with the 10^{-13} factor applying to all three.

Table A3. Signed changes in peak magnitude relative to U0 (%).

Case	Field	x	y	z
UE	Displacement	12.8541	12.8454	12.4972
UE	Electric field	−4.6960	−4.6921	5.4030
UK	Displacement	0.0425	0.0410	0.0302
UK	Electric field	0.4473	0.4473	−0.0492
UT	Displacement	−0.0006	−0.0010	−0.0068
UT	Electric field	0.6340	0.6339	−0.0755

In UE, the sampled displacement maxima shift by 0.008 s in x and y and 0.006 s in z; the electric maxima shift by 0.020 s in all three components. UK and UT retain the sampled peak times in every recorded component. No dominant-peak sign switch is inferred for these revised comparisons.

Table A4. Electric differences in the 3.5–5.0 s window and maximum full-record vertical residual magnitude. Residuals use the full-record U0 peak; windowed D_2 uses the U0 norm within the window. Time identifies the maximum vertical residual in the electric display coordinate.

Case	$D_2(E_x)$ (%)	$D_2(E_y)$ (%)	$D_2(E_z)$ (%)	max $\lvert\delta E_z\rvert$ (%)	Time (s)
UE	129.968	129.946	132.921	63.409	4.16
UK	2.741	2.741	2.896	1.268	4.08
UT	10.490	10.489	10.950	4.975	4.76

For UT, the 1.6–2.8 s electric window gives D_2 = 1.238%, 1.232% and 1.445% for E_x, E_y and E_z, respectively. The maximum full-record vertical displacement residual is 0.1370% of the U0 peak. Large windowed percentages mainly reflect the small U0 norm within the selected interval, so their amplitude significance was assessed together with the absolute peaks and full-record measures.

References

1. Pride, S. Governing equations for the coupled electromagnetics and acoustics of porous media. *Phys. Rev. B* **1994**, *50*, 15678–15696. [CrossRef]
2. Chen, B.; Mu, Y. Experimental studies of seismoelectric effects in fluid-saturated porous media. *J. Geophys. Eng.* **2005**, *2*, 222–230. [CrossRef]

3. Gao, Y.; Zhao, G.; Chong, J.; Klemperer, S.L.; Han, B.; Jiang, F.; Wen, J.; Chen, X.; Zhan, Y.; Tang, J.; et al. Coseismic electric and magnetic signals observed during 2017 Jiuzhaigou M_w 6.5 earthquake and explained by electrokinetics and magnetometer rotation. *Geophys. J. Int.* **2020**, *223*, 1130–1143. [CrossRef]
4. Ren, H.; Huang, Q.; Chen, X. Numerical simulation of seismo-electromagnetic fields associated with a fault in a porous medium. *Geophys. J. Int.* **2016**, *206*, 205–220. [CrossRef]
5. Sun, Y.C.; Uyeshima, M.; Ren, H.; Huang, Q.; Aizawa, K.; Tsukamoto, K.; Kanda, W.; Seki, K.; Kishita, T.; Ohminato, T.; et al. Numerical simulations to explain the coseismic electromagnetic signals: A case study for a M5.4 aftershock of the 2016 Kumamoto earthquake. *Earth Planets Space* **2019**, *71*, 143. [CrossRef]
6. Cheng, Q.; Gao, Y.; Zhou, G.; Chen, C.H.; Wang, D.; Yao, C. Expected electromagnetic response from natural earthquakes in a layered ocean model. *Geophys. J. Int.* **2025**, *240*, 1667–1689. [CrossRef]
7. Haartsen, M.W.; Pride, S.R. Electroseismic waves from point sources in layered media. *J. Geophys. Res.* **1997**, *102*, 24745–24769. [CrossRef]
8. Garambois, S.; Dietrich, M. Full waveform numerical simulations of seismoelectromagnetic wave conversions in fluid-saturated stratified porous media. *J. Geophys. Res.* **2002**, *107*, ESE 5-1–ESE 5-18. [CrossRef]
9. Haines, S.S.; Pride, S.R. Seismoelectric numerical modeling on a grid. *Geophysics* **2006**, *71*, N57–N65. [CrossRef]
10. Gao, Y.; Huang, F.; Hu, H. Comparison of full and quasi-static seismoelectric analytically based modeling. *J. Geophys. Res. Solid Earth* **2017**, *122*, 8066–8106. [CrossRef]
11. Ji, Y.; Han, L.; Huang, X.; Zhao, X.; Jensen, K.; Yu, Y. A high-order finite-difference scheme for time-domain modeling of time-varying seismoelectric waves. *Geophysics* **2022**, *87*, T135–T146. [CrossRef]
12. Li, J.; Yin, C.; Liu, Y.; Wang, L.; Ma, X. Simulation of seismoelectric waves using time-domain finite-element method in 2D PSVTM mode. *Remote Sens.* **2023**, *15*, 3321. [CrossRef]
13. Li, J.; Yin, C.; Su, Y.; Zhang, B.; Ren, X.; Liu, Y. Three-Dimensional Time-Domain Finite-Element Modeling of Seismoelectric Waves. *IEEE Trans. Geosci. Remote Sens.* **2025**, *63*, 5901414. [CrossRef]
14. Bucher, F.; Zyserman, F.I.; Monachesi, L.B. Numerical modelling of seismoelectric signals for offshore exploration. *J. Appl. Geophys.* **2025**, *243*, 105925. [CrossRef]
15. Bernardo, N.; Martins-Gomes, V.; Bordes, C.; Brito, D. Seismoelectric Conversion at Poroelastic/Elastic Interfaces and the Role of Dielectric Permittivity: Experimental and Numerical Analysis. *Geophys. Res. Lett.* **2024**, *51*, e2024GL112994. [CrossRef]
16. Martins-Gomes, V.; Brito, D.; Garambois, S.; Dietrich, M.; Bordes, C.; Barucq, H. The effect of layer thickness and fluid conductivity contrasts on seismoelectric signals: Insights from laboratory experiments and numerical simulations. *Geophys. J. Int.* **2026**, *245*, ggag065. [CrossRef]
17. Thomsen, L. Weak elastic anisotropy. *Geophysics* **1986**, *51*, 1954–1966. [CrossRef]
18. Cheng, A.H.D. Material coefficients of anisotropic poroelasticity. *Int. J. Rock Mech. Min. Sci.* **1997**, *34*, 199–205. [CrossRef]
19. Zhu, Z.; Toksöz, M.N.; Zhan, X. Seismoelectric measurements in a porous quartz-sand sample with anisotropic permeability. *Geophys. Prospect.* **2016**, *64*, 700–713. [CrossRef]
20. Tohti, M.; Wang, Y.; Slob, E.; Zheng, Y.; Chang, X.; Yao, Y. Seismoelectric numerical simulation in 2D vertical transverse isotropic poroelastic medium. *Geophys. Prospect.* **2020**, *68*, 1927–1943. [CrossRef]
21. Tohti, M.; Wang, Y.; Xiao, W.; Zhou, K. Numerical simulation of seismoelectric wavefields in 3D orthorhombic poroelastic medium. *Chin. J. Geophys.* **2022**, *65*, 4471–4484. (In Chinese with English abstract)
22. Han, L.; Ji, Y.; Ye, W.; Wang, S.; Lin, J.; Huang, X. Seismoelectric wave propagation simulation by combining poro-viscoelastic anisotropic model with Cole–Cole depression model. *IEEE Trans. Geosci. Remote Sens.* **2022**, *60*, 4510910. [CrossRef]
23. Han, L.; Huang, X.; Quintal, B.; Ji, Y.; Sun, T. Seismoelectric Wave Propagation in Velocity and Attenuation Anisotropic Media. *IEEE Trans. Geosci. Remote Sens.* **2024**, *62*, 4514010. [CrossRef]
24. Liu, P.; An, Z.; Fan, Y.; Lin, Y.; He, Y.; Hou, Y. A Hybrid Spectral-Element and Finite-Element Framework for Three-Dimensional Full-Wave Seismoelectric Modeling. *Geosciences* **2026**, *16*, 413. [CrossRef]
25. Biot, M.A. Theory of Propagation of Elastic Waves in a Fluid-Saturated Porous Solid. I. Low-Frequency Range. *J. Acoust. Soc. Am.* **1956**, *28*, 168–178. [CrossRef]
26. Morency, C.; Tromp, J. Spectral-element simulations of wave propagation in porous media. *Geophys. J. Int.* **2008**, *175*, 301–345. [CrossRef]
27. SPECFEM Developers. SPECFEM3D Cartesian: Open-Source Spectral-Element Software for Three-Dimensional Seismic Wave Propagation. Software Description and Developer Attribution in the README and src/specfem3D/specfem3D.F90. 2026. Available online: https://github.com/SPECFEM/specfem3d (accessed on 30 October 2026).
28. Amestoy, P.R.; Duff, I.S.; L'Excellent, J.Y.; Koster, J. A fully asynchronous multifrontal solver using distributed dynamic scheduling. *SIAM J. Matrix Anal. Appl.* **2001**, *23*, 15–41. [CrossRef]
29. Clayton, R.; Engquist, B. Absorbing boundary conditions for acoustic and elastic wave equations. *Bull. Seismol. Soc. Am.* **1977**, *67*, 1529–1540. [CrossRef]

30. SPECFEM Developers. SPECFEM3D Cartesian: Poroelastic Moment-Tensor Source Implementation. Source Assembly, Source-Time Function, and Moment-Tensor Input Routines in src/specfem3D; Public Implementation Inspected at Commit 7a1c764. 2024. Available online: https://github.com/SPECFEM/specfem3d (accessed on 27 October 2026).
31. Hu, H.; Gao, Y. Electromagnetic field generated by a finite fault due to electrokinetic effect. *J. Geophys. Res. Solid Earth* **2011**, *116*, B08302. [CrossRef]
32. Aminzadeh, F.; Burkhard, N.; Nicoletis, L.; Rocca, F.; Wyatt, K. SEG/EAEG 3-D modeling project: 2nd update. *Lead. Edge* **1994**, *13*, 949–952. [CrossRef]
33. Peng, R.; Di, B.; Glover, P.W.J.; Wei, J.; Lorinczi, P.; Liu, Z.; Li, H. Seismo-electric conversion in shale: Experiment and analytical modelling. *Geophys. J. Int.* **2020**, *223*, 725–745. [CrossRef]
34. Grobbe, N.; Slob, E.C. Seismo-electromagnetic thin-bed responses: Natural signal enhancements? *J. Geophys. Res. Solid Earth* **2016**, *121*, 2460–2479. [CrossRef]
35. Wapenaar, K. Unified matrix–vector wave equation, reciprocity and representations. *Geophys. J. Int.* **2019**, *216*, 560–583. [CrossRef]
36. Sen, P.N.; Goode, P.A. Influence of temperature on electrical conductivity on shaly sands. *Geophysics* **1992**, *57*, 89–96. [CrossRef]
37. Aoyama, K.; Hashimoto, T. Numerical Simulation on the Electrical Conductivity of Ternary Mixtures Containing NaCl Solution, Quartz, and Smectite. *J. Geophys. Res. Solid Earth* **2024**, *129*, e2024JB029063. [CrossRef]
38. Pride, S.R.; Morgan, F.D. Electrokinetic dissipation induced by seismic waves. *Geophysics* **1991**, *56*, 914–925. [CrossRef]
39. Wang, W.; Gao, W.; Liu, J.; Kundu, T.; Cui, Z. The Response Mechanism of Borehole Shear-Horizontal Transverse-Electric Seismoelectric Waves to Fluid Salinity. *Appl. Sci.* **2022**, *12*, 5132. [CrossRef]
40. Revil, A.; Glover, P.W.J. Nature of surface electrical conductivity in natural sands, sandstones, and clays. *Geophys. Res. Lett.* **1998**, *25*, 691–694. [CrossRef]
41. Bíró, O.; Preis, K. On the use of the magnetic vector potential in the finite-element analysis of three-dimensional eddy currents. *IEEE Trans. Magn.* **1989**, *25*, 3145–3159. [CrossRef]

Disclaimer/Publisher's Note: The statements, opinions and data contained in all publications are solely those of the individual author(s) and contributor(s) and not of MDPI and/or the editor(s). MDPI and/or the editor(s) disclaim responsibility for any injury to people or property resulting from any ideas, methods, instructions or products referred to in the content.